PHYSICAL REVIEW A **83**, 053811 (2011)

Self-consistent Maxwell-Bloch theory of quantum-dot-population switching in photonic crystals

Hiroyuki Takeda
Department of Physics, University of Toronto, 60 St. George Street, Toronto, Ontario M5S 1A7, Canada, and
International Center for Young Scientists, National Institute for Materials Science, 1-2-1 Sengen, Tsukuba, Ibaraki, Japan 305-0047

Sajeev John
Department of Physics, University of Toronto, 60 St. George Street, Toronto, Ontario M5S 1A7, Canada,

(Received 11 January 2011; published 9 May 2011)

We theoretically demonstrate the population switching of quantum dots (QD's), modeled as two-level atoms in idealized one-dimensional (1D) and two-dimensional (2D) photonic crystals (PC's) by self-consistent solution of the Maxwell-Bloch equations. In our semiclassical theory, energy states of the electron are quantized, and electron dynamics is described by the atomic Bloch equation, while electromagnetic waves satisfy the classical Maxwell equations. Near a waveguide cutoff in a photonic band gap, the local electromagnetic density of states (LDOS) and spontaneous emission rates exhibit abrupt changes with frequency, enabling large QD population inversion driven by both continuous and pulsed optical fields. We recapture and generalize this ultrafast population switching using the Maxwell-Bloch equations. Radiative emission from the QD is obtained directly from the surrounding PC geometry using finite-difference time-domain simulation of the electromagnetic field. The atomic Bloch equations provide a source term for the electromagnetic field. The total electromagnetic field, consisting of the external input and radiated field, drives the polarization components of the atomic Bloch vector. We also include a microscopic model for phonon dephasing of the atomic polarization and nonradiative decay caused by damped phonons. Our self-consistent theory captures stimulated emission and coherent feedback effects of the atomic Mollow sidebands, neglected in earlier treatments. This leads to remarkable high-contrast QD-population switching with relatively modest (factor of 10) jump discontinuities in the electromagnetic LDOS. Switching is demonstrated in three separate models of QD's placed (i) in the vicinity of a band edge of a 1D PC, (ii) near a cutoff frequency in a bimodal waveguide channel of a 2D PC, and (iii) in the vicinity of a localized defect mode side coupled to a single-mode waveguide channel in a 2D PC.

DOI: 10.1103/PhysRevA.83.053811 PACS number(s): 42.70.Qs, 32.80.−t

I. INTRODUCTION

Photonic crystals (PC's) are artificial periodic dielectric materials capable of localizing light, providing very strong light-matter coupling, and enabling engineering of the electromagnetic density of states. In a photonic band gap (PBG), light in a certain frequency range cannot propagate due to destructive wave interference in all spatial directions [1–3]. Point and line defects in PBG materials correspond to localized modes and waveguides of light, respectively [4,5]. Remarkable subwavelength circuit paths for light with sharp bends and near-perfect transmission over a broad bandwidth can be realized in a PBG with single-mode waveguides. Moreover, a combination of cavities and waveguides enables filtering light with a certain frequency [6,7]. These properties enable functional three-dimensional integrated optics [8–12].

PBG materials also enable control of spontaneous emission of light [2]. The rate of spontaneous emission is determined by the local density of states (LDOS) of photons (Purcell effect) in the vicinity of the emitting atom [11,12]. In conventional materials, the LDOS is constant or monotonically increasing with frequency. In a PBG material, however, the LDOS can be made orders of magnitude larger or smaller than in conventional materials over large volumes. While LDOS's inside PBG's may vanish, those near photonic band edges can be dramatically enhanced. In other words, spontaneous emission can be greatly inhibited and greatly enhanced within adjacent frequency intervals in a PBG material [12].

Moreover, abrupt changes of LDOS can be combined with very strong light-matter coupling in a PC to enable population inversion of two-level atoms driven by external continuous waves [12–14] and optical pulses [15,16]. When electrons are resonantly excited by external light with the frequency ω_L, populations at ground and excited states oscillate with the Rabi frequency, 2Ω, defined by dipole coupling energy of the field to the atom. The emission spectrum exhibits three frequency components of ω_L and $\omega_L \pm 2\Omega$ (Mollow triplet) [17]. When strong coupling is combined with large contrast of LDOS's at $\omega_L \pm 2\Omega$, population inversion can be achieved with low-power external light.

Previous studies of atomic population switching and inversion have considered simplified models of either the atomic response or the field electrodynamics. Initial studies [18] demonstrate collective atomic switching for a steady-state applied field, with an assumed LDOS profile without any specific PBG waveguide geometry. This was then generalized to steady-state switching of a collection of independent inhomogeneously broadened quantum dots (QD's) distributed in a PBG waveguide geometry. Here electromagnetic wave propagation in the waveguide was simulated by the finite-difference time-domain (FDTD) method, but the atomic response was described by a steady-state susceptibility and an assumed LDOS profile [19]. This demonstrated the validity of QD-population switching for optical pulse control using realistic optical power levels and QD parameters. A more microscopic picture of atomic Bloch vector dynamics reveals

[15,16] a remarkable, high-contrast dynamic switching effect with nearly complete atomic inversion long after the exciting optical pulse has subsided. This suggests the possibility of on-chip optical information processing and multiwavelength channel all-optical transistor action. However, this study utilized an assumed LDOS profile rather than an electromagnetic reservoir resulting from a specific dielectric geometry surrounding the QD's.

In this paper, we provide a fully self-consistent description of QD Bloch vector dynamics, electromagnetic wave propagation, and electromagnetic LDOS. No assumption is made about the LDOS profile in the vicinity of the QD. Instead, the density of modes and the mode spatial profile emerge from FDTD simulation of the wave field in specific dielectric geometries. In our self-consistent, microscopic model, the total electromagnetic wave field (consisting of external optical pulses and radiation from the QD's) acts as a driving term for atomic Bloch vector dynamics. The quantum expectation value of the oscillating atomic polarization, in turn, acts as a source term for the electromagnetic field. The self-consistent solution of these coupled Maxwell-Bloch equations reveals important features not present in earlier treatments. The Mollow spectrum of the radiating QD appears naturally from the power spectrum of the radiating dipole. When one of the Mollow sidebands is pushed into a spectral range of high LDOS caused by the onset of slow-group-velocity modes in the PC, radiative emission at the corresponding frequency is enhanced. Moreover, as emitted light accumulates in the slow modes of the waveguide cavity, stimulated emission takes place, further amplifying emission from relevant Mollow components. Our self-consistent theory with coherent feedback reveals ultrafast, high-contrast population switching with much smaller jump discontinuities in the LDOS than previously anticipated [12–16,18–20].

Whereas earlier studies have assumed a ratio of spontaneous emission rates of well over 100 between the lower and upper QD Mollow sidebands, the Maxwell-Bloch theory reveals that similar switching effects can be achieved with LDOS jumps of roughly a factor of 10. Physically, this occurs because stimulated emission effectively amplifies the radiative emission rate ratio relative to the dielectric-structure-induced LDOS ratio between the Mollow sidebands. As a result, QD-based population switching and control of light with light is much more robust than previously recognized. In particular, this suggests that our switching effect may be accessible in present-day 2D membrane photonic crystals. We also introduce a microscopic model for dipole dephasing and nonradiative decay of the QD Bloch vector arising from interaction with acoustic phonons in the PC backbone. In the event that a polaronic cloud can form more rapidly than the Bloch vector responds to the surrounding electromagnetic fields, the effective transition dipole of the QD is reduced by the Frank-Condon effect. In the event that the phonons themselves decay by anharmonic processes, nonradiative decay occurs.

For numerical analysis of PC's, the plane-wave expansion (PWE) [21] and FDTD methods [22] are powerful tools for obtaining photonic band structures and electromagnetic field dynamics, respectively. Electrons and electromagnetic waves satisfy the atomic Bloch [23] and Maxwell equations, respectively. Solving these two equations self-consistently, we can obtain time-dependent populations of electrons at ground and excited states. We use FDTD to solve the Maxwell-Bloch equations [24–27]. In the Maxwell-Bloch equations we do not require any ansatz for the electromagnetic LDOS. Instead, we simply set up structural parameters for concrete PC geometries and place two-level atoms at specific positions. We demonstrate that most radiative emissions can be recaptured by the Maxwell-Bloch equations without recourse to any phenomenological spontaneous emission decay terms.

We consider electrons in QD's as particles in boxes with dimensions of $L_x \times L_y \times L_z$. Energy states of QD's are controlled by these lengths. When electric fields are polarized in the z direction, the transition energy between ground and excited states depends only on L_z. In one-dimensional (1D) PC's, dielectric multilayer stacks are described as modulated dielectrics in the x direction and infinite in the yz plane. In our terminology, QD's at $x = x'$ refer to QD's distributed in the yz plane at $x = x'$. Accordingly, we must consider the areal density of QD's in the yz plane. We refer to these QD distributions as QD layers. In two-dimensional (2D) PC's, dielectric pillars are described as modulated dielectrics in the xy plane and infinite in the z direction. QD's at $(x,y) = (x',y')$ refer to dots distributed in the z direction at $(x,y) = (x',y')$. We consider the linear density of QD's in the z direction. We refer to these QD distributions as the QD rods.

In this paper, we consider specific 1D and 2D PC's for the sake of numerical convenience. More realistic architectures suited for fabrication and optical experiments (and requiring considerably more computational time) will be discussed elsewhere. Our model systems, nevertheless, provide the correct qualitative picture. One-dimensional PC's are composed of planar SiO_2 layers in the air, and a QD layer is distributed inside a SiO_2 layer. The QD layer is excited by external light propagating normal to 1D stacks. We choose 2D PC's composed of GaN circular rods arrayed in a square lattice in an air background. This exhibits a large PBG for transverse magnetic (TM) modes propagating perpendicular to the rod axes with electric field in the z direction. To introduce a bimodal waveguide in the 2D PC, one row of rods is completely removed (air mode), and an adjacent row is composed of dielectric rods with smaller radii (dielectric mode). Two guided modes then appear inside the PBG. An LDOS jump occurs when the dielectric mode has a cutoff frequency inside the PBG. A QD rod is inserted in place of one rod of the dielectric mode. The QD rod is evanescently excited by light propagation through the adjacent air mode. We also consider a single-mode air waveguide with a side-coupled defect consisting of a smaller dielectric rod. A QD rod is distributed inside this smaller dielectric rod. Here the localized defect mode is associated with a sharp modulation of the electromagnetic LDOS near the QD transition frequency.

This paper is organized as follows. In Sec. II, we formulate the Maxwell-Bloch equations, including radiative emission and phonon dephasing, and discuss computational methods for solving this system of nonlinear equations self-consistently. We also discuss QD energy spectra and how the electromagnetic LDOS can be inferred from the FDTD simulation of the wave field. In Sec. III, we present our numerical results for various PC model systems and discuss their interpretation. Section IV contains our overall conclusions.

II. MAXWELL-BLOCH EQUATIONS

A. Quantum-dot Bloch equation

1. Radiative coupling without dephasing

QD's with ground and excited states, with energies $\hbar\omega_1$ and $\hbar\omega_2$, respectively, are considered as two-level atoms. We use the Heisenberg equations of motion for the atomic operators:

$$\frac{dc_i(t)}{dt} = -\frac{i}{\hbar}[c_i(t),H], \tag{1}$$

where $c_i(t) = e^{iHt/\hbar}c_i e^{-iHt/\hbar}$, c_i and $c_i^\dagger$ are the electron annihilation and creation operators, respectively, at the ground ($i = 1$) or excited ($i = 2$) state, and $H = H_A - \mathbf{d}\cdot\mathbf{E}(t) = \hbar\omega_A c_2^\dagger c_2 - \mathbf{d}_0\cdot\mathbf{E}(t)(c_1^\dagger c_2 + c_2^\dagger c_1)$. The annihilation and creation operators satisfy the fermionic anticommutation algebra $\{c_i,c_j^\dagger\} = c_i c_j^\dagger + c_j^\dagger c_i = \delta_{ij}$ and $\{c_i,c_j\} = c_i c_j + c_j c_i = 0$ ($i,j = 1,2$). H_A is the Hamiltonian of the two-level atom, $\omega_A = \omega_2 - \omega_1$ is the atomic frequency, $\mathbf{d} = -e\mathbf{r}$ is the electric dipole of the atom, $\mathbf{d}_0 = \langle 1|\mathbf{d}|2\rangle = \langle 2|\mathbf{d}|1\rangle$ is real, and $\mathbf{E}(t)$ is the electric field. Equation (1) yields

$$\frac{dc_1(t)}{dt} = i\frac{\mathbf{d_0}\cdot\mathbf{E}(t)}{\hbar}c_2(t) \tag{2}$$

$$\frac{dc_2(t)}{dt} = -i\omega_A c_2(t) + i\frac{\mathbf{d_0}\cdot\mathbf{E}(t)}{\hbar}c_1(t). \tag{3}$$

Likewise, it follows that

$$\frac{dc_1^\dagger(t)c_2(t)}{dt} = -i\omega_A c_1^\dagger(t)c_2(t) - i\frac{\mathbf{d_0}\cdot\mathbf{E}(t)}{\hbar}[c_2^\dagger(t)c_2(t) - c_1^\dagger(t)c_1(t)] \tag{4}$$

$$\frac{dc_1^\dagger(t)c_1(t)}{dt} = i\frac{\mathbf{d_0}\cdot\mathbf{E}(t)}{\hbar}[c_1^\dagger(t)c_2(t) - c_2^\dagger(t)c_1(t)] = -\frac{dc_2^\dagger(t)c_2(t)}{dt}. \tag{5}$$

$c_1^\dagger(t)c_1(t) + c_2^\dagger(t)c_2(t) = 1$ (= const) is satisfied since $d[c_1^\dagger(t)c_1(t) + c_2^\dagger(t)c_2(t)]/dt = 0$. We define the operators $\sigma_1(t) = c_1^\dagger(t)c_2(t) + c_2^\dagger(t)c_1(t)$, $\sigma_2(t) = i[c_1^\dagger(t)c_2(t) - c_2^\dagger(t)c_1(t)]$, and $\sigma_3(t) = c_2^\dagger(t)c_2(t) - c_1^\dagger(t)c_1(t) = 2c_2^\dagger(t)c_2(t) - 1$. Taking averages of the operators $\langle\sigma_i(t)\rangle = \mathrm{tr}[\rho\sigma_i(t)] = \sum_{n=1}^{2}\langle n|\rho\sigma_i(t)|n\rangle$, where ρ is the atomic density operator, $\langle c_1^\dagger(t)c_1(t)\rangle$ and $\langle c_2^\dagger(t)c_2(t)\rangle$ indicate the populations at the ground and excited states, respectively. Then, we obtain

$$\frac{d}{dt}\begin{bmatrix}\langle\sigma_1(t)\rangle\\ \langle\sigma_2(t)\rangle\\ \langle\sigma_3(t)\rangle\end{bmatrix} = \begin{bmatrix}0 & -\omega_A & 0\\ \omega_A & 0 & 2\mathbf{d}_0\cdot\mathbf{E}(t)/\hbar\\ 0 & -2\mathbf{d}_0\cdot\mathbf{E}(t)/\hbar & 0\end{bmatrix}\begin{bmatrix}\langle\sigma_1(t)\rangle\\ \langle\sigma_2(t)\rangle\\ \langle\sigma_3(t)\rangle\end{bmatrix}. \tag{6}$$

Equation (6) is called the atomic Bloch Equation [23]. In the absence of radiative or phonon-mediated damping or dephasing, $\langle\sigma_1(t)\rangle^2 + \langle\sigma_2(t)\rangle^2 + \langle\sigma_3(t)\rangle^2 = \langle\sigma_1^{\mathrm{eq}}\rangle^2 + \langle\sigma_2^{\mathrm{eq}}\rangle^2 + \langle\sigma_3^{\mathrm{eq}}\rangle^2 =$ const, where $\langle\sigma_i^{\mathrm{eq}}\rangle = \mathrm{tr}[\rho^{\mathrm{eq}}\sigma_i]$ ($i = 1,2,3$). $\rho^{\mathrm{eq}} = e^{-H_A/k_BT}/\mathrm{tr}[e^{-H_A/k_BT}]$ is the density operator in thermal equilibrium, where k_B and T are the Boltzmann factor and temperature, respectively. Then, $\langle\sigma_1^{\mathrm{eq}}\rangle = 0$, $\langle\sigma_2^{\mathrm{eq}}\rangle = 0$, and $\langle\sigma_3^{\mathrm{eq}}\rangle = [e^{-\hbar\omega_A/k_BT} - 1]/[e^{-\hbar\omega_A/k_BT} + 1]$. At zero temperature ($T = 0$ K), $\langle\sigma_3^{\mathrm{eq}}\rangle = -1$. Even at room temperature ($T = 300$ K), $\langle\sigma_3^{\mathrm{eq}}\rangle \simeq -1$ when ω_A corresponds to the wavelength $\lambda_A = 1.5$ μm. In this case, we consider $\langle\sigma_1(t)\rangle^2 + \langle\sigma_2(t)\rangle^2 + \langle\sigma_3(t)\rangle^2 = 1$ (probability conservation law). The electric dipole per QD is defined by $\langle\mathbf{d}(t)\rangle = -\langle\partial H/\partial\mathbf{E}(t)\rangle = \mathbf{d}_0\langle\sigma_1(t)\rangle$. In what follows, we will consider the temporal oscillations of this dipole as a source term in Maxwell's equations. This captures aspects of spontaneous emission and stimulated emission from the atom as it radiates in response to an external field or in response to previously emitted light, trapped in an optical cavity mode near the atom. In a colored electromagnetic vacuum, with a steplike jump in the LDOS, this stimulated emission effectively enhances the disparity between the spontaneous emission rates on either side of the discontinuity. Before discussing this effect in detail, we consider the role of additional interactions of the atom with its environment. One of these is the coupling of the QD to lattice vibrations of the host semiconductor. The resulting dipole dephasing effects, together with random spontaneous emission, allow the QD Bloch vector to explore the interior of the unit Bloch sphere during its dynamical evolution. The state of the QD is no longer a pure quantum state, but rather a statistical mixture.

2. Phonon dephasing with undamped phonons

We first consider the influence of undamped phonons with infinite lifetime. Lattice vibrations interact with the QD to induce small, rapidly fluctuating shifts in the ground-to-excited-state transition energy and diminish the QD dipole as it evolves in the Bloch sphere. The following Hamiltonian includes the QD-phonon interaction [28]:

$$H = \hbar\omega_A c_2^\dagger c_2 - \mathbf{d}_0\cdot\mathbf{E}(t)(c_1^\dagger c_2 + c_2^\dagger c_1) + \sum_{\mathbf{q}}\eta_{\mathbf{q}}(b_{\mathbf{q}}^\dagger c_2^\dagger c_2 + c_2^\dagger c_2 b_{\mathbf{q}}) + \sum_{\mathbf{q}}\hbar\omega_{\mathbf{q}}b_{\mathbf{q}}^\dagger b_{\mathbf{q}}, \tag{7}$$

where $\mathbf{q}$ is the phonon wave vector, $\omega_{\mathbf{q}}$ is the phonon frequency, $\eta_{\mathbf{q}}$ is the electron-phonon interaction coefficient, and $b_{\mathbf{q}}$ and $b_{\mathbf{q}}^\dagger$ are the annihilation and creation operators of phonons, respectively ($[b_{\mathbf{q}},b_{\mathbf{q}}^\dagger] = 1$). $b_{\mathbf{q}}(t)$ satisfies the Heisenberg equation of motion, $\frac{db_{\mathbf{q}}(t)}{dt} = -i\omega_{\mathbf{q}}b_{\mathbf{q}}(t) - i\frac{\eta_{\mathbf{q}}}{\hbar}c_2^\dagger(t)c_2(t) \simeq -i\omega_{\mathbf{q}}b_{\mathbf{q}}(t)$. (Conventionally, the second term is neglected for simplicity, although $\eta_{\mathbf{q}}$ is larger than $\hbar\omega_{\mathbf{q}}$ at a certain $|\mathbf{q}|$ [28].) Then, $b_{\mathbf{q}}(t) = b_{\mathbf{q}}e^{-i\omega_{\mathbf{q}}t}$ (independent boson model). Using the polaron transformation $\hat{H} = e^X He^{-X}$, where $X = \sum_{\mathbf{q}}\frac{\eta_{\mathbf{q}}}{\hbar\omega_q}(b_{\mathbf{q}}^\dagger c_2^\dagger c_2 - c_2^\dagger c_2 b_{\mathbf{q}})$, we obtain $\hat{H} = \hbar(\omega_A - \Delta)c_2^\dagger c_2 - \mathbf{d}_0\cdot\mathbf{E}(t)(c_1^\dagger D_- c_2 + c_2^\dagger D_+ c_1) + \sum_{\mathbf{q}}\hbar\omega_{\mathbf{q}}b_{\mathbf{q}}^\dagger b_{\mathbf{q}}$, where $\Delta = \sum_{\mathbf{q}}\frac{\eta_{\mathbf{q}}^2}{\hbar^2\omega_{\mathbf{q}}}$ is the polaron shift and

$D_\pm = \exp[\pm \sum_{\mathbf{q}} \frac{\eta_{\mathbf{q}}}{\hbar\omega_q}(b_{\mathbf{q}}^\dagger - b_{\mathbf{q}})]$ are lattice displacement operators. Then, $H = e^{-X}\hat{H}e^{X}$ is rewritten as

$$H = \hbar(\omega_A - \Delta)\tilde{c}_2^\dagger\tilde{c}_2 - \mathbf{d}_0\cdot\mathbf{E}(t)(\tilde{c}_1^\dagger D_-\tilde{c}_2 + \tilde{c}_2^\dagger D_+\tilde{c}_1) + \sum_{\mathbf{q}}\hbar\omega_{\mathbf{q}}\tilde{b}_{\mathbf{q}}^\dagger\tilde{b}_{\mathbf{q}}, \tag{8}$$

where $\tilde{c}_1 = e^{-X}c_1e^{X} = c_1$, $\tilde{c}_2 = e^{-X}c_2e^{X} = D_+c_2$, and $\tilde{b}_{\mathbf{q}} = e^{-X}b_{\mathbf{q}}e^{X} = b_{\mathbf{q}} + \frac{\eta_{\mathbf{q}}}{\hbar\omega_{\mathbf{q}}}c_2^\dagger c_2$. The polaron-transformed atomic Bloch vector component operators are $\langle\tilde{\sigma}_i(t)\rangle = \langle\sigma_i(t)\rangle$ since $\tilde{c}_1^\dagger D_-\tilde{c}_2 = c_1^\dagger c_2$ and $\tilde{c}_2^\dagger D_+\tilde{c}_1 = c_2^\dagger c_1$. On the other hand, $e^{-X}D_\pm e^{X} = \exp[\pm\sum_{\mathbf{q}}\frac{\eta_{\mathbf{q}}}{\hbar\omega_q}(\tilde{b}_{\mathbf{q}}^\dagger - \tilde{b}_{\mathbf{q}})] = \exp[\pm\sum_{\mathbf{q}}\frac{\eta_{\mathbf{q}}}{\hbar\omega_q}(b_{\mathbf{q}}^\dagger - b_{\mathbf{q}})] = D_\pm$. The Heisenberg Equation (1) yields

$$\frac{d\tilde{c}_1(t)}{dt} = i\frac{\mathbf{d_0}\cdot\mathbf{E}(t)}{\hbar}D_-(t)\tilde{c}_2(t) \tag{9}$$

$$\frac{d\tilde{c}_2(t)}{dt} = -i(\omega_A - \Delta)\tilde{c}_2(t) + i\frac{\mathbf{d_0}\cdot\mathbf{E}(t)}{\hbar}D_+(t)\tilde{c}_1(t). \tag{10}$$

Then, $\tilde{c}_1^\dagger(t)\tilde{c}_1(t) = c_1^\dagger(t)c_1(t)$ and $\tilde{c}_2^\dagger(t)\tilde{c}_2(t) = c_2^\dagger(t)c_2(t)$ satisfy

$$\begin{aligned}\frac{d\tilde{c}_1^\dagger(t)\tilde{c}_1(t)}{dt} &= i\frac{\mathbf{d_0}\cdot\mathbf{E}(t)}{\hbar}[\tilde{c}_1^\dagger(t)D_-(t)\tilde{c}_2(t) - \tilde{c}_2^\dagger(t)D_+(t)\tilde{c}_1(t)]\\ &= -\frac{d\tilde{c}_2^\dagger(t)\tilde{c}_2(t)}{dt},\end{aligned} \tag{11}$$

so that $\tilde{c}_1^\dagger(t)\tilde{c}_1(t) + \tilde{c}_2^\dagger(t)\tilde{c}_2(t) = 1(= \text{const})$ is satisfied.

Using $\tilde{c}_1^\dagger(t) = \tilde{c}_1^\dagger(0) - i\int_0^t d\tau\frac{\mathbf{d_0}\cdot\mathbf{E}(\tau)}{\hbar}\tilde{c}_2^\dagger(\tau)D_+(\tau)$ and $\tilde{c}_2(t) = \tilde{c}_2(0)e^{-i(\omega_A-\Delta)t} + i\int_0^t d\tau e^{-i(\omega_A-\Delta)(t-\tau)}\frac{\mathbf{d_0}\cdot\mathbf{E}(\tau)}{\hbar}D_+(\tau)\tilde{c}_1(\tau)$, we obtain the quantum expectation value (see the Appendix) of the polaron-transformed atomic deexcitation operator $\langle\tilde{\sigma}_-(t)\rangle = [\langle\tilde{\sigma}_1(t)\rangle - i\langle\tilde{\sigma}_2(t)\rangle]/2 = \langle\tilde{c}_1^\dagger(t)D_-(t)\tilde{c}_2(t)\rangle$:

$$\begin{aligned}\langle\tilde{\sigma}_-(t)\rangle &= \langle\tilde{c}_1^\dagger(0)D_-(t)\tilde{c}_2(0)\rangle e^{-i(\omega_A-\Delta)t}\\ &\quad -i\int_0^t d\tau e^{-i(\omega_A-\Delta)(t-\tau)}\frac{\mathbf{d_0}\cdot\mathbf{E}(\tau)}{\hbar}\\ &\quad \times[\langle\tilde{c}_2^\dagger(\tau)D_+(\tau)D_-(t)\tilde{c}_2(\tau)\rangle\\ &\quad -\langle\tilde{c}_1^\dagger(\tau)D_-(t)D_+(\tau)\tilde{c}_1(\tau)\rangle]\\ &\simeq \langle\tilde{c}_1^\dagger(0)D_-(t)\tilde{c}_2(0)\rangle e^{-i(\omega_A-\Delta)t}\\ &\quad -i\int_0^t d\tau e^{-i(\omega_A-\Delta)(t-\tau)}\frac{\mathbf{d_0}\cdot\mathbf{E}(\tau)}{\hbar}\\ &\quad \times[\langle D_+(\tau)D_-(t)\rangle\langle\tilde{c}_2^\dagger(\tau)\tilde{c}_2(\tau)\rangle\\ &\quad -\langle D_-(t)D_+(\tau)\rangle\langle\tilde{c}_1^\dagger(\tau)\tilde{c}_1(\tau)\rangle]\\ &= \langle\tilde{c}_1^\dagger(0)D_-(t)\tilde{c}_2(0)\rangle e^{-i(\omega_A-\Delta)t}\\ &\quad -i\int_0^t d\tau e^{-i(\omega_A-\Delta)(t-\tau)}\frac{\mathbf{d_0}\cdot\mathbf{E}(\tau)}{\hbar}\\ &\quad \times[e^{R(\tau-t)-S}\langle\tilde{c}_2^\dagger(\tau)\tilde{c}_2(\tau)\rangle\\ &\quad -e^{R(t-\tau)-S}\langle\tilde{c}_1^\dagger(\tau)\tilde{c}_1(\tau)\rangle].\end{aligned} \tag{12}$$

From the viewpoint of the independent boson model, $\langle D_\pm(t_1)D_\mp(t_2)\rangle = e^{R(t_1-t_2)-S}$, where $R(t) = \sum_{\mathbf{q}}\frac{\eta_{\mathbf{q}}^2}{\hbar^2\omega_{\mathbf{q}}^2}[(n_{\mathbf{q}}+1)e^{-i\omega_{\mathbf{q}}t} + n_{\mathbf{q}}e^{i\omega_{\mathbf{q}}t}]$ and $S = R(0) = \sum_{\mathbf{q}}\frac{\eta_{\mathbf{q}}^2}{\hbar^2\omega_{\mathbf{q}}^2}(2n_{\mathbf{q}}+1)$ are phonon dynamics and the Huang-Rhys factor, respectively [29]. $n_{\mathbf{q}} = \langle b_{\mathbf{q}}^\dagger b_{\mathbf{q}}\rangle = 1/[\exp(\hbar\omega_{\mathbf{q}}/k_BT) - 1]$ is the thermal Bose-Einstein distribution. In the above, we have used the mean-field factorization $\langle\tilde{c}_2^\dagger(\tau)D_+(\tau)D_-(t)\tilde{c}_2(\tau)\rangle \simeq \langle D_+(\tau)D_-(t)\rangle\langle\tilde{c}_2^\dagger(\tau)\tilde{c}_2(\tau)\rangle$ and $\langle\tilde{c}_1^\dagger(\tau)D_-(t)D_+(\tau)\tilde{c}_1(\tau)\rangle \simeq \langle D_-(t)D_+(\tau)\rangle\langle\tilde{c}_1^\dagger(\tau)\tilde{c}_1(\tau)\rangle$.

If $|\Psi\rangle = |1\rangle$ (ground state), then $\tilde{c}_2(0)|\Psi\rangle = 0$, whereas if $|\Psi\rangle = |2\rangle$ (excited state), then $\langle\Psi|\tilde{c}_1^\dagger(0) = 0$. Therefore, in what follows, we set $\langle\tilde{c}_1^\dagger(0)D_-(t)\tilde{c}_2(0)\rangle = 0$.

When inputting the δ-pulse electric field $\mathbf{E}(t) = \mathbf{E}_0\delta(t)$ in the absence of spontaneous emission, $\langle\tilde{\sigma}_-(t)\rangle = -i(\mathbf{d}_0\cdot\mathbf{E}_0/\hbar)e^{-i(\omega_A-\Delta)t}[e^{R(-t)-S}\langle\tilde{c}_2^\dagger(0)\tilde{c}_2(0)\rangle - e^{R(t)-S}\langle\tilde{c}_1^\dagger(0)\tilde{c}_1(0)\rangle]\Theta(t)$, where $\Theta(t) = 1$ for $t > 0$ and $\Theta(t) = 0$ for $t < 0$. When initial states are ground and excited states, $\langle\tilde{\sigma}_-(t)\rangle = i(\mathbf{d}_0\cdot\mathbf{E}_0/\hbar)e^{-i(\omega_A-\Delta)t}e^{R(t)-S}$ and $-i(\mathbf{d}_0\cdot\mathbf{E}_0/\hbar)e^{-i(\omega_A-\Delta)t}e^{R(-t)-S}$, respectively. From $\langle\mathbf{d}(t)\rangle = -\langle\partial H/\partial\mathbf{E}(t)\rangle = \mathbf{d}_0[\langle\tilde{\sigma}_-(t)\rangle + \langle\tilde{\sigma}_+(t)\rangle] = \mathbf{d}_0\langle\tilde{\sigma}_1(t)\rangle$, the electric dipole oscillates with $e^{-i(\omega_A-\Delta)t}e^{R(\pm t)-S}$, and this oscillation becomes $e^{-i(\omega_A-\Delta)t}e^{-S}$ after sufficient time has elapsed $[R(\pm t)\to 0]$. This means that undamped phonons weaken the dipole oscillation but the dipole keeps oscillating. When initial states are ground and excited states, absorption and emission occur, respectively. Therefore, dipole oscillations of $e^{-i(\omega_A-\Delta)t}e^{R(t)-S}$ and $e^{-i(\omega_A-\Delta)t}e^{R(-t)-S}$ correspond to those of the absorption and emission, respectively.

We consider the spectral decomposition of the thermal phonon dynamics $g_\pm(t) = e^{-i(\omega_A-\Delta)t+R(\pm t)-S} = \int_{-\infty}^{\infty}d\omega g_\pm(\omega)e^{-i\omega t}$, where $g_+(\omega)$ and $g_-(\omega)$ can be interpreted as the absorption and emission line shapes due to phonon dephasing with undamped phonons, respectively, in the absence of spontaneous emission.

$$\begin{aligned}g_\pm(\omega) &= \frac{1}{2\pi}\int_{-\infty}^{\infty}dt e^{i(\omega-\omega_A+\Delta)t+R(\pm t)-S}\\ &= \frac{1}{\pi}\mathrm{Re}\left[\int_0^{\infty}dt e^{i(\omega-\omega_A+\Delta)t+R(\pm t)-S}\right]\\ &= e^{-S}\delta(\omega-\omega_A+\Delta)\\ &\quad +\frac{e^{-S}}{\pi}\mathrm{Re}\left\{\int_0^{\infty}dt e^{i(\omega-\omega_A+\Delta)t}[e^{R(\pm t)}-1]\right\}\end{aligned} \tag{13}$$

with $\int_{-\infty}^{\infty}d\omega g_\pm(\omega) = 1$. The second term on the right-hand side of Eq. (13) can be calculated numerically by the fast Fourier transform. $g_\pm(\omega)$ are real and temperature dependent and, in the absence of spontaneous emission, have a sharp peak at $\omega = \omega_A - \Delta$ and a broad phonon dephasing peak near $\omega = \omega_A - \Delta$. We define $g_s(\omega) = [g_+(\omega) + g_-(\omega)]/2$ and $g_a(\omega) = [g_+(\omega) - g_-(\omega)]/2$, where $g_s(\omega)$ and $g_a(\omega)$ are symmetric and antisymmetric, respectively, with respect to $\omega = \omega_A - \Delta$.

We define $F_{a,s}(t,\omega) \equiv -i\int_0^t d\tau e^{-i\omega(t-\tau)}\frac{\mathbf{d_0}\cdot\mathbf{E}(\tau)}{\hbar}[\langle\tilde{c}_2^\dagger(\tau)\tilde{c}_2(\tau)\rangle \pm \langle\tilde{c}_1^\dagger(\tau)\tilde{c}_1(\tau)\rangle]$. For $F_a(t,\omega)$, the quantity in square brackets reduces to unity, $\langle\tilde{c}_1^\dagger(\tau)\tilde{c}_1(\tau)\rangle + \langle\tilde{c}_2^\dagger(\tau)\tilde{c}_2(\tau)\rangle = 1$, whereas, for $F_s(t,\omega)$, the quantity in square brackets is

$\langle\sigma_3(\tau)\rangle = \langle\tilde{c}_2^\dagger(\tau)\tilde{c}_2(\tau)\rangle - \langle\tilde{c}_1^\dagger(\tau)\tilde{c}_1(\tau)\rangle$. It follows from Eq. (12) and the above definitions that

$$\langle\tilde{\sigma}_-(t)\rangle = \int_{-\infty}^{\infty} d\omega[g_s(\omega)F_s(t,\omega) - g_a(\omega)F_a(t,\omega)]. \qquad (14)$$

We have used $g_\pm(\omega) = g_s(\omega) \pm g_a(\omega)$. Actually, the first term on the right-hand side of Eq. (14) is much larger than the second term.

$$\frac{dF_{a,s}(t,\omega)}{dt} = -i\omega F_{a,s}(t,\omega) - i\frac{\mathbf{d_0}\cdot\mathbf{E}(t)}{\hbar}[\langle\tilde{c}_2^\dagger(t)\tilde{c}_2(t)\rangle \pm \langle\tilde{c}_1^\dagger(t)\tilde{c}_1(t)\rangle]. \qquad (15)$$

Introducing the notation $\langle\sigma_1(t)\rangle_{s,a}^{(\omega)} = 2\text{Re}[F_{s,a}(t,\omega)]$, $\langle\sigma_2(t)\rangle_{s,a}^{(\omega)} = -2\text{Im}[F_{s,a}(t,\omega)]$, we obtain

$$\frac{d\langle\sigma_1(t)\rangle_{s,a}^{(\omega)}}{dt} = -\omega\langle\sigma_2(t)\rangle_{s,a}^{(\omega)} \qquad (16)$$

$$\frac{d\langle\sigma_2(t)\rangle_{s}^{(\omega)}}{dt} = \omega\langle\sigma_1(t)\rangle_{s}^{(\omega)} + 2\frac{\mathbf{d_0}\cdot\mathbf{E}(t)}{\hbar}\langle\sigma_3(t)\rangle \qquad (17)$$

$$\frac{d\langle\sigma_2(t)\rangle_{a}^{(\omega)}}{dt} = \omega\langle\sigma_1(t)\rangle_{a}^{(\omega)} + 2\frac{\mathbf{d_0}\cdot\mathbf{E}(t)}{\hbar} \qquad (18)$$

$$\frac{d\langle\sigma_3(t)\rangle}{dt} = -2\frac{\mathbf{d_0}\cdot\mathbf{E}(t)}{\hbar} \times \left[\int_{-\infty}^{\infty} d\omega g_s(\omega)\langle\sigma_2(t)\rangle_s^{(\omega)} - \int_{-\infty}^{\infty} d\omega g_a(\omega)\langle\sigma_2(t)\rangle_a^{(\omega)}\right]. \qquad (19)$$

It follows from the consideration after Eq. (11) that $\langle\sigma_i(t)\rangle = [\int_{-\infty}^{\infty} d\omega g_s(\omega)\langle\sigma_i(t)\rangle_s^{(\omega)} - \int_{-\infty}^{\infty} d\omega g_a(\omega)\langle\sigma_i(t)\rangle_a^{(\omega)}]$ $(i = 1,2)$. Equations (16)–(19) correspond to the atomic Bloch equation including phonon dephasing in the absorption and emission processes. A physical meaning of these equations is that we assign a weight function $g_\pm(\omega)$ that the transition frequency of QD's is shifted from ω_A to ω due to phonon dephasing. In the case of dynamic phonon-mediated broadening, $\langle\sigma_1(t)\rangle^2 + \langle\sigma_2(t)\rangle^2 + \langle\sigma_3(t)\rangle^2 \leqslant 1$. In other words, the QD Bloch vector explores the interior of the unit sphere due to phonon dephasing.

3. Damped phonons and nonradiative relaxation

Dephasing by infinitely-long-lived phonons reduces the atomic polarization but does not cause decay of the excited QD to its ground state. If the phonons have a finite lifetime due to anharmonic decay to lower-frequency phonons, this provides a microscopic mechanism for nonradiative decay. To describe this effect, we introduce a phenomenological decay in which the time-dependent annihilation and creation phonon operators satisfy $b_{\mathbf{q}}(t) = b_{\mathbf{q}}e^{-i\omega_{\mathbf{q}}t-\gamma_{\mathbf{q}}|t|}$ and $b_{\mathbf{q}}^\dagger(t) = b_{\mathbf{q}}^\dagger e^{i\omega_{\mathbf{q}}t-\gamma_{\mathbf{q}}|t|}$. From the independent boson model, it can be shown [30] that $\langle D_\pm(t_1)D_\mp(t_2)\rangle = e^{-\Gamma_{\text{damp}}|t_1-t_2|}e^{\bar{R}(t_1-t_2)-\bar{S}(t_1-t_2)}$, where

$$\Gamma_{\text{damp}} = \sum_{\mathbf{q}} \frac{\eta_{\mathbf{q}}^2\gamma_{\mathbf{q}}}{\hbar^2(\omega_{\mathbf{q}}^2+\gamma_{\mathbf{q}}^2)}(2n_{\mathbf{q}}+1). \qquad (20)$$

$\bar{R}(t) = \sum_{\mathbf{q}} \frac{\eta_{\mathbf{q}}^2}{\hbar^2}[(n_{\mathbf{q}}+1)\frac{e^{-i\omega_{\mathbf{q}}t-\gamma_{\mathbf{q}}t}}{(\omega_{\mathbf{q}}-i\gamma_{\mathbf{q}})^2} + n_{\mathbf{q}}\frac{e^{i\omega_{\mathbf{q}}t-\gamma_{\mathbf{q}}t}}{(\omega_{\mathbf{q}}+i\gamma_{\mathbf{q}})^2}]\Theta(t) + \sum_{\mathbf{q}} \frac{\eta_{\mathbf{q}}^2}{\hbar^2}[(n_{\mathbf{q}}+1)\frac{e^{-i\omega_{\mathbf{q}}t+\gamma_{\mathbf{q}}t}}{(\omega_{\mathbf{q}}+i\gamma_{\mathbf{q}})^2} + n_{\mathbf{q}}\frac{e^{i\omega_{\mathbf{q}}t+\gamma_{\mathbf{q}}t}}{(\omega_{\mathbf{q}}-i\gamma_{\mathbf{q}})^2}]\Theta(-t)$ and $\bar{S}(t) = \sum_{\mathbf{q}} \frac{\eta_{\mathbf{q}}^2}{\hbar^2}[\frac{n_{\mathbf{q}}+1}{(\omega_{\mathbf{q}}-i\gamma_{\mathbf{q}})^2} + \frac{n_{\mathbf{q}}}{(\omega_{\mathbf{q}}+i\gamma_{\mathbf{q}})^2}]\Theta(t) + \sum_{\mathbf{q}} \frac{\eta_{\mathbf{q}}^2}{\hbar^2}[\frac{n_{\mathbf{q}}+1}{(\omega_{\mathbf{q}}+i\gamma_{\mathbf{q}})^2} + \frac{n_{\mathbf{q}}}{(\omega_{\mathbf{q}}-i\gamma_{\mathbf{q}})^2}]\Theta(-t) = \bar{S}_+\Theta(t) + \bar{S}_-\Theta(-t)$ are the modified phonon dynamics and Huang-Rhys factor, respectively. Unlike in undamped phonons, the modified Huang-Rhys factor $\bar{S}_\pm$ is not real but complex. Although conventionally $t > 0$ is assumed, we consider both $t > 0$ and $t < 0$ for the discussion of absorption and emission line shapes. Then, Eq. (12) is modified as follows:

$$\langle\tilde{\sigma}_-(t)\rangle \to -i\int_0^t d\tau e^{-i(\omega_A-\bar{\Delta})(t-\tau)-\Gamma_{\text{damp}}(t-\tau)}\frac{\mathbf{d_0}\cdot\mathbf{E}(\tau)}{\hbar} \times [e^{\bar{R}(\tau-t)-\bar{S}(\tau-t)}\langle\tilde{c}_2^\dagger(\tau)\tilde{c}_2(\tau)\rangle - e^{\bar{R}(t-\tau)-\bar{S}(t-\tau)}\langle\tilde{c}_1^\dagger(\tau)\tilde{c}_1(\tau)\rangle], \qquad (21)$$

where $\bar{\Delta} = \sum_{\mathbf{q}} \frac{\eta_{\mathbf{q}}^2\omega_{\mathbf{q}}}{\hbar^2(\omega_{\mathbf{q}}^2+\gamma_{\mathbf{q}}^2)}$ and we have used the previously discussed properties of $\tilde{c}_2(0)$ and $\tilde{c}_1^\dagger(0)$. This means that the electric dipole oscillates with $e^{-i(\omega_A-\bar{\Delta})t-\Gamma_{\text{damp}}t}e^{\bar{R}(\pm t)-\bar{S}(\pm t)}$, and this oscillation decays to zero after sufficient time has elapsed, unlike in the case of undamped phonons. Even in the absence of radiative spontaneous emission, the QD excitation energy is completely dissipated via damped phonons. We note also that the phonon damping parameters $\gamma_{\mathbf{q}}$ reduce the polaronic frequency shift $\bar{\Delta}$ and also restrain the Frank-Condon transition matrix element overlap effects $e^{-\bar{S}_\pm}$ between the polaronic excited state and ground state.

The absorption and emission line shapes due to phonon dephasing with damped phonons become [following the same steps leading to Eq. (13)]

$$\begin{aligned} g_\pm(\omega) &= \frac{1}{2\pi}\int_{-\infty}^{\infty} dt e^{i(\omega-\omega_A+\bar{\Delta})t-\Gamma_{\text{damp}}|t|+\bar{R}(\pm t)-\bar{S}(\pm t)} \\ &= \text{Re}\left[\frac{e^{-\bar{S}_\pm}}{\pi}\frac{\Gamma_{\text{damp}}+i(\omega-\omega_A+\bar{\Delta})}{(\omega-\omega_A+\bar{\Delta})^2+\Gamma_{\text{damp}}^2}\right] \\ &\quad +\frac{1}{\pi}\text{Re}\left\{\int_0^\infty dt e^{i(\omega-\omega_A+\bar{\Delta})t-\Gamma_{\text{damp}}t}e^{-\bar{S}_\pm} \times [e^{\bar{R}(\pm t)}-1]\right\}, \end{aligned} \qquad (22)$$

with $\int_{-\infty}^{\infty} d\omega g_\pm(\omega) = 1$. With increasing Γ_{damp}, $g_\pm(\omega)$ becomes broader. However, we need a very fine mesh of frequencies to accurately describe the first term (sharp peak) on the right-hand side of Eq. (22) for small Γ_{damp}. In analogy to Eq. (13),

$$\begin{aligned} \bar{g}_\pm(\omega) &= \frac{1}{2\pi}\int_{-\infty}^{\infty} dt e^{i(\omega-\omega_A+\bar{\Delta})t+\bar{R}(\pm t)-\bar{S}(\pm t)} \\ &= \text{Re}\left\{e^{-\bar{S}_\pm}\left[\delta(\omega-\omega_A+\bar{\Delta})+\frac{i}{\pi}P\left(\frac{1}{\omega-\omega_A+\bar{\Delta}}\right)\right]\right\} \\ &\quad +\frac{1}{\pi}\text{Re}\left\{\int_0^\infty dt e^{i(\omega-\omega_A+\bar{\Delta})t}e^{-\bar{S}_\pm}[e^{\bar{R}(\pm t)}-1]\right\}, \end{aligned} \qquad (23)$$

with $\int_{-\infty}^{\infty} d\omega\bar{g}_\pm(\omega) = 1$ and P being the principal value. Using $\bar{g}_s(\omega) = [\bar{g}_+(\omega) + \bar{g}_-(\omega)]/2$ and $\bar{g}_a(\omega) = [\bar{g}_+(\omega) - \bar{g}_-(\omega)]/2$, we introduce the spectral decomposition of

$\langle\sigma_i(t)\rangle = \int_{-\infty}^{\infty} d\omega \bar{g}_s(\omega)\langle\bar{\sigma}_i(t)\rangle_s^{(\omega)} - \int_{-\infty}^{\infty} d\omega \bar{g}_a(\omega)\langle\bar{\sigma}_i(t)\rangle_a^{(\omega)}$ for $i = 1,2$. In analogy to Eq. (14), we introduce

$$\langle\tilde{\sigma}_-(t)\rangle = \int_{-\infty}^{\infty} d\omega[\bar{g}_s(\omega)\bar{F}_s(t,\omega) - \bar{g}_a(\omega)\bar{F}_a(t,\omega)], \quad (24)$$

where $\bar{F}_{a,s}(t,\omega) = -i\int_0^t d\tau e^{-i\omega(t-\tau)-\Gamma_{\text{damp}}(t-\tau)}\frac{\mathbf{d_0}\cdot\mathbf{E}(\tau)}{\hbar}[\langle\tilde{c}_2^\dagger(\tau)\tilde{c}_2(\tau)\rangle \pm \langle\tilde{c}_1^\dagger(\tau)\tilde{c}_1(\tau)\rangle]$ satisfy relations analogous to Eq. (15):

$$\frac{d\bar{F}_{a,s}(t,\omega)}{dt} = [-i\omega - \Gamma_{\text{damp}}]\bar{F}_{a,s}(t,\omega) - i\frac{\mathbf{d_0}\cdot\mathbf{E}(t)}{\hbar}[\langle\tilde{c}_2^\dagger(t)\tilde{c}_2(t)\rangle \pm \langle\tilde{c}_1^\dagger(t)\tilde{c}_1(t)\rangle]. \quad (25)$$

Introducing the notation $\langle\bar{\sigma}_1(t)\rangle_{s,a}^{(\omega)} = 2\text{Re}[\bar{F}_{s,a}(t,\omega)]$ and $\langle\bar{\sigma}_2(t)\rangle_{s,a}^{(\omega)} = -2\text{Im}[\bar{F}_{s,a}(t,\omega)]$ leads to the following ansatz for atomic Bloch vector dynamics in the presence of phonon dephasing with damped, finite-lifetime phonons:

$$\frac{d\langle\bar{\sigma}_1(t)\rangle_{s,a}^{(\omega)}}{dt} = -\Gamma_{\text{damp}}\langle\bar{\sigma}_1(t)\rangle_{s,a}^{(\omega)} - \omega\langle\bar{\sigma}_2(t)\rangle_{s,a}^{(\omega)} \quad (26)$$

$$\frac{d\langle\bar{\sigma}_2(t)\rangle_{s}^{(\omega)}}{dt} = \omega\langle\bar{\sigma}_1(t)\rangle_{s}^{(\omega)} - \Gamma_{\text{damp}}\langle\bar{\sigma}_2(t)\rangle_{s}^{(\omega)} + 2\frac{\mathbf{d_0}\cdot\mathbf{E}(t)}{\hbar}\langle\sigma_3(t)\rangle \quad (27)$$

$$\frac{d\langle\bar{\sigma}_2(t)\rangle_{a}^{(\omega)}}{dt} = \omega\langle\bar{\sigma}_1(t)\rangle_{a}^{(\omega)} - \Gamma_{\text{damp}}\langle\bar{\sigma}_2(t)\rangle_{a}^{(\omega)} + 2\frac{\mathbf{d_0}\cdot\mathbf{E}(t)}{\hbar} \quad (28)$$

$$\frac{d\langle\sigma_3(t)\rangle}{dt} = -2\frac{\mathbf{d_0}\cdot\mathbf{E}(t)}{\hbar}\left[\int_{-\infty}^{\infty} d\omega\bar{g}_s(\omega)\langle\bar{\sigma}_2(t)\rangle_s^{(\omega)} - \int_{-\infty}^{\infty} d\omega\bar{g}_a(\omega)\langle\bar{\sigma}_2(t)\rangle_a^{(\omega)}\right] - \Gamma_{\text{pop}}[\langle\sigma_3(t)\rangle + 1] \quad (29)$$

The first term on the right-hand side of Eq. (29) describes radiative suppression of the atomic population in the presence of damped phonon sidebands. However, this by itself does not force the atomic Bloch vector to reach the ground state in all cases in the long-time limit. It has been shown in a full quantum theory [30] that, even in the presence of complete 3D PBG's, coupling to damped, finite-lifetime acoustic phonons leads to a decay of the atomic excited-state population to zero. In order to recapture the correct physical behavior in our model, we introduce a phenomenological decay rate Γ_{pop}, This parameter is influenced by the polarization decay rate Γ_{damp} but may be smaller than Γ_{damp} due to Frank-Condon displacement of the excited atomic state from its ground state due to the surrounding phonon cloud. In our numerical studies, we choose Γ_{damp} and Γ_{pop} in a manner consistent with experimental observations.

As in this case of phonon dephasing, for damped phonons, $\langle\sigma_1(t)\rangle^2 + \langle\sigma_2(t)\rangle^2 + \langle\sigma_3(t)\rangle^2 \leqslant 1$, and the QD Bloch vector probes the interior of the unit sphere. In Eqs. (26)–(29), radiative decay is influenced by the reduction of effective transition dipole by phonon-mediated dephasing and the Frank-Condon factor $e^{-\bar{S}_\pm}$ arising from polaronic shift of the excited-state wave function. These effects are, in turn, weakened by the finite lifetime of the phonons comprising the polaronic cloud around the QD. Our model also provides a mechanism for nonradiative relaxation through the parameter Γ_{pop} and the parameter Γ_{damp} that is determined [see Eq. (20)] by the electron-phonon coupling parameter $n_{\mathbf{q}}$, the phonon dispersion $\omega_{\mathbf{q}}$, and the phonon damping rates $\gamma_{\mathbf{q}}$.

In the atomic Bloch equation, $\langle\sigma_3(t)\rangle$ defines the nature of population inversion. When $\langle\sigma_3(t)\rangle > 0$, population inversion is achieved. In Eqs. (6), (16)–(19), and (26)–(29), $\mathbf{E}(t)$ includes the input electric field $\mathbf{E}_{\text{in}}(t)$ and the electric field radiated from the two-level atom $\mathbf{E}_{\text{rad}}(t)$. $\mathbf{E}_{\text{rad}}(t)$ describes spontaneous and stimulated emission. Conventionally, the term including $\mathbf{E}_{\text{rad}}(t)$ is replaced for the phenomenological decay term of spontaneous emission [23]. In this paper, however, no such phenomenological decay terms are attached since we calculate $\mathbf{E}(t)$ [$= \mathbf{E}_{\text{in}}(t) + \mathbf{E}_{\text{rad}}(t)$] by Maxwell equations. In this way, features of the structured electromagnetic vacuum are automatically probed by the Maxwell-Bloch equations. There is no need to include different phenomenological radiative decay parameters $\gamma_\pm$ for spontaneous emission in high- and low-density-of-states regions as done previously [12–16,18,19]. We note, however, that spontaneous emission in our model occurs only if the atomic dipole is activated. In our simulation, this condition is satisfied since QD is interacting with a strong external optical pulse. In the event that such an external trigger mechanism is not present, it is necessary to introduce a randomly fluctuating noise term in the equation of motion for the atomic operators. Such a noise term has been described previously [31] in the context of a structured electromagnetic reservoir. Vacuum fluctuation can be replaced by a classical noise function. In other words, it involves a stochastic function: $\mathbf{E}_{\text{vac}}(t) = \sum_{n=1}^{N}\mathbf{E}_n\cos(\omega_n t + \Phi_n)$, where ω_n is the discrete frequency and Φ_n is the random phase. When $N \to \infty$, the ensemble of $\mathbf{E}_{\text{vac}}(t)$ converges to zero, $\langle\mathbf{E}_{\text{vac}}(t)\rangle_{\text{ens}} = 0$, because of the sum of random phases. On the other hand, the expansion coefficient $\mathbf{E}_n$ is chosen to satisfy that $\langle\mathbf{E}_{\text{vac}}(t)\cdot\mathbf{E}_{\text{vac}}(t')\rangle_{\text{ens}}$ coincides with the underlying temporal autocorrelation of a quantum noise operator [31]. Adding $\mathbf{E}_{\text{vac}}(t)$ to $\mathbf{E}(t)$, we can incorporate the vacuum fluctuation in the Maxwell-Bloch equation. Our damped phonon model with phenomenological population decay parameter Γ_{pop} provides decay that supersedes vacuum fluctuations and allows us to circumvent these subtleties with a simple model.

B. Maxwell equations with electric polarizations

Electromagnetic fields $\mathbf{E}(\mathbf{r};t)$ and $\mathbf{H}(\mathbf{r};t)$ satisfy the Maxwell equations.

$$\nabla\times\mathbf{E}(\mathbf{r};t) = -\mu_0\frac{\partial\mathbf{H}(\mathbf{r};t)}{\partial t}, \quad (30)$$

$$\nabla\times\mathbf{H}(\mathbf{r};t) = \mathbf{J}(\mathbf{r};t) + \sigma(\mathbf{r})\mathbf{E}(\mathbf{r};t) + \epsilon_0\epsilon(\mathbf{r})\frac{\partial\mathbf{E}(\mathbf{r};t)}{\partial t}, \quad (31)$$

where

$$\mathbf{J}(\mathbf{r};t) = \frac{\partial\mathbf{P}(\mathbf{r};t)}{\partial t}. \quad (32)$$

ϵ_0($= 8.854\times10^{-12}$ F/m) and μ_0($= 4\pi\times10^{-7}$ H/m) are the permittivity and permeability, respectively, in vacuum. Here, $\sigma(\mathbf{r})$ is the conductivity and $\epsilon(\mathbf{r})$ is the dielectric constant determined by the dielectric microstructure. $\mathbf{J}(\mathbf{r};t)$ is the electric current density. The electric polarization $\mathbf{P}(\mathbf{r};t)$ is defined by $\mathbf{P}(\mathbf{r};t) = N(\mathbf{r})\langle\mathbf{d}(t)\rangle = N(\mathbf{r})\mathbf{d}_0\langle\sigma_1(t)\rangle$, $[\langle\mathbf{d}(t)\rangle = -\langle\partial H/\partial\mathbf{E}(\mathbf{r};t)\rangle = \mathbf{d}_0\langle\sigma_1(t)\rangle]$. In our self-consistent numerical simulations, $\langle\sigma_1(t)\rangle$ is determined from Eqs. (6), (16)–(19), and (26)–(29) and the defining spectral decomposition equations (14) and (24). $N(\mathbf{r})$ is the number of QD's per volume and depends on the dimensionality of the specific PC model:

$$N(\mathbf{r}) = \begin{cases} N_A\delta(x-x') & (1\mathrm{D}) \\ N_L\delta(x-x')\delta(y-y') & (2\mathrm{D}) \\ N_P\delta(x-x')\delta(y-y')\delta(z-z') & (3\mathrm{D}) \end{cases}. \qquad (33)$$

In our 1D model PC, N_A is the areal density of QD's in the yz plane at $x = x'$ (QD layer). In the 2D PC, N_L is the linear density of QD's in the z direction at $(x,y) = (x',y')$ (QD rod). In 3D crystals, N_P is the point density or the number of QD's at $(x,y,z) = (x',y',z')$. While Eqs. (6), (16)–(19), and (26)–(29), include $\mathbf{E}(t) = \mathbf{E}(\mathbf{r}';t)$, Eq. (31) includes $\langle\sigma_1(t)\rangle$ as a source term. In other words, we obtain the time-dependent $\langle\sigma_3(t)\rangle$ by solving the atomic Bloch and Maxwell equations self-consistently. Maxwell equations are solved numerically by discretization with respect to time and space, according to the FDTD method. In this paper, we treat 1D and 2D PC's. While $\Delta x/a = 1/50$ and $c\Delta t/a = 1/100$ in 1D PC's , $\Delta x/a = \Delta y/a = 1/20$ and $c\Delta t/a = 1/40$ in 2D PC's , where a is the lattice constant of the PC and c is the speed of light in a vacuum.

C. Local electromagnetic densities of states

LDOS's are necessary for the discussion of spontaneous emission and population inversion of QD's in PC's. We describe here our method of calculating LDOS's by the FDTD method. We focus on the 1D and 2D TM modes. When $J_z(\mathbf{r},\mathbf{r}';t) = \delta(\mathbf{r}-\mathbf{r}')S(t)$ and $\sigma(\mathbf{r}) = 0.0$ in Eqs. (30) and (31), the electric field in the z direction E_z satisfies

$$\left[-\frac{\partial^2}{\partial t^2} + \frac{c^2}{\epsilon(\mathbf{r})}\nabla^2\right]E_z(\mathbf{r},\mathbf{r}';t) = \frac{1}{\epsilon_0\epsilon(\mathbf{r})}\delta(\mathbf{r}-\mathbf{r}')\frac{\partial S(t)}{\partial t}. \qquad (34)$$

In what follows we choose a Gaussian impulse $S(t) = S_0 e^{-\beta(t-t')^2}$ as our source in the time domain. Fourier transforming $E_z(\mathbf{r},\mathbf{r}';t)$ and $S(t)$ to $E_z(\mathbf{r},\mathbf{r}';\omega) = \int_0^\infty dt e^{i\omega t}E_z(\mathbf{r},\mathbf{r}';t)$ and $S(\omega) = \int_0^\infty dt e^{i\omega t}S(t)$, respectively, Eq. (34) becomes

$$\left[\omega^2 + \frac{c^2}{\epsilon(\mathbf{r})}\nabla^2\right]E_z(\mathbf{r},\mathbf{r}';\omega) = -i\frac{\omega}{\epsilon_0\epsilon(\mathbf{r})}\delta(\mathbf{r}-\mathbf{r}')S(\omega). \qquad (35)$$

$S(\omega) \simeq S_0\sqrt{\pi/\beta}e^{i\omega t'}e^{-\omega^2/(4\beta)}$. When $\beta = \omega_0^2/(4\ln 2)$, $|S(\omega = \omega_0)| = |S(\omega = 0)|/2$. We choose $\omega_0 a/2\pi c = 0.5$, where a is the lattice constant. We take $e^{-\beta t'^2} = 10^{-6}$.

From $-\frac{c^2}{\epsilon(\mathbf{r})}\nabla^2 E_{z\lambda}(\mathbf{r}) = \omega_\lambda^2 E_{z\lambda}(\mathbf{r})$ and $\sum_\lambda E_{z\lambda}(\mathbf{r})E_{z\lambda}^*(\mathbf{r}') = \frac{V}{\epsilon(\mathbf{r})}\delta(\mathbf{r}-\mathbf{r}')$, where ω_λ and $E_{z\lambda}(\mathbf{r})$ are the eigenvalues and eigenvectors, respectively, and V is the volume, Eq. (35) becomes

$$E_z(\mathbf{r},\mathbf{r}';\omega) = -i\frac{S(\omega)}{2\epsilon_0 V}\sum_\lambda\left[\frac{1}{\omega-\omega_\lambda} + \frac{1}{\omega+\omega_\lambda}\right] \times E_{z\lambda}(\mathbf{r})E_{z\lambda}^*(\mathbf{r}'). \qquad (36)$$

The physical electric field amplitude is obtained from $\lim_{\delta\to 0}E_z(\mathbf{r},\mathbf{r}';\omega+i\delta) = \lim_{\delta\to 0}\int_0^\infty dt e^{-\delta t}e^{i\omega t}E_z(\mathbf{r},\mathbf{r}';t)$. This leads to a relation between the field and the local electromagnetic density of states as follows:

$$\begin{aligned} E_z(\mathbf{r},\mathbf{r}';\omega) &= \lim_{\delta\to 0}E_z(\mathbf{r},\mathbf{r}';\omega+i\delta) \\ &= -i\frac{S(\omega)}{2\epsilon_0 V}\lim_{\delta\to 0}\sum_\lambda\left[\frac{1}{\omega-\omega_\lambda+i\delta} + \frac{1}{\omega+\omega_\lambda+i\delta}\right] \\ &\quad\times E_{z\lambda}(\mathbf{r})E_{z\lambda}^*(\mathbf{r}') \\ &= -\frac{S(\omega)}{2\epsilon_0 V}\sum_\lambda \pi\{\delta(\omega-\omega_\lambda) + \delta(\omega+\omega_\lambda)\} \\ &\quad\times E_{z\lambda}(\mathbf{r})E_{z\lambda}^*(\mathbf{r}') + i\frac{S(\omega)}{2\epsilon_0 V}\sum_\lambda\left\{P\left(\frac{1}{\omega-\omega_\lambda}\right)\right. \\ &\quad\left. + P\left(\frac{1}{\omega+\omega_\lambda}\right)\right\}E_{z\lambda}(\mathbf{r})E_{z\lambda}^*(\mathbf{r}'). \end{aligned} \qquad (37)$$

We have used $\lim_{\delta\to 0}\frac{1}{x+i\delta} = P(\frac{1}{x}) - i\pi\delta(x)$. Then, the LDOS at $\mathbf{r} = \mathbf{r}'$ is

$$\begin{aligned} \rho_{\mathrm{LDOS}}(\omega;\mathbf{r}') &= \frac{1}{V}\sum_\lambda[\delta(\omega-\omega_\lambda) + \delta(\omega+\omega_\lambda)]|E_{z\lambda}(\mathbf{r}')|^2 \\ &= -\frac{2\epsilon_0}{\pi}\mathrm{Re}\left[\frac{E_z(\mathbf{r}',\mathbf{r}';\omega)}{S(\omega)}\right]. \end{aligned} \qquad (38)$$

In the FDTD method, we apply the Gaussian impulse $J_z(\mathbf{r},\mathbf{r}';t) = \delta(\mathbf{r}-\mathbf{r}')S(t)$, detect the electric field at $\mathbf{r} = \mathbf{r}'$, and Fourier transform it with respect to time. This is the $E_z(\mathbf{r}',\mathbf{r}';\omega)$ in Eq. (38). In this way, we obtain the LDOS at $\mathbf{r} = \mathbf{r}'$.

D. Quantum dots with two levels

We consider a particle-in-a-box model for the QD with the potential energy $V(x,y,z) = 0$ for $|x| \leqslant L_x/2$, $|y| \leqslant L_y/2$, and $|z| \leqslant L_z/2$. Otherwise, $V(x,y,z) = \infty$. Then, energies and wave functions are as follows:

$$E_{n_x n_y n_z} = \frac{\hbar^2}{2m}\left[\left(\frac{n_x\pi}{L_x}\right)^2 + \left(\frac{n_x\pi}{L_y}\right)^2 + \left(\frac{n_x\pi}{L_z}\right)^2\right] \qquad (39)$$

$$(n_{x,y,z} = 1,2,\ldots) \quad \text{and}$$

$$\psi_{n_x n_y n_z}(x,y,z) = \phi_{n_x}(x)\phi_{n_y}(y)\phi_{n_z}(z), \qquad (40)$$

where

$$\phi_{n_\xi}(\xi) = \begin{cases} \sqrt{\frac{2}{L_\xi}}\cos\left(\frac{n_\xi\pi}{L_\xi}\xi\right) & (n_\xi = \text{odd}) \\ \sqrt{\frac{2}{L_\xi}}\sin\left(\frac{n_\xi\pi}{L_\xi}\xi\right) & (n_\xi = \text{even}) \end{cases} \qquad (41)$$

for $|x| \leqslant L_x/2$, $|y| \leqslant L_y/2$, and $|z| \leqslant L_z/2$. Otherwise, $\psi_{n_x n_y n_z}(x,y,z) = 0$. m is the effective mass of electrons. Although the ground state is E_{111}, three states of E_{211}, E_{121}, and E_{112} are considered as the excited states. In this paper, we consider electric fields polarized in the z direction. In Eqs. (6), (16)–(19), and (26)–(29), then, $\mathbf{d}_0\cdot\mathbf{E} = d_{0z}E_z = -ez_0E_z$. To obtain interactions of dipoles and electric fields, $z_0 = \langle 1|z|2\rangle = \langle 2|z|1\rangle$ should be nonzero. Therefore, we take $|1\rangle = \psi_{111}(x,y,z)$ and $|2\rangle = \psi_{112}(x,y,z)$. Then, $z_0 = (16/9\pi^2)L_z$. When $|2\rangle = \psi_{211}(x,y,z)$ or $\psi_{121}(x,y,z)$, $z_0 = 0.0$. The transition energy is $\Delta E = E_{112} - E_{111} = 3\hbar^2\pi^2/2mL_z^2 = \hbar\omega_A$ and

$L_z = L = \sqrt{3\pi^2\hbar/2m\omega_A}$. In this model, the transition energy of QD's depends only on L_z, whereas L_x and L_y do not affect the energy gap when electric fields are polarized in the z direction. In what follows, we consider $L_x = L_y = L_z = L$ (cubic model). The above situation can be realized by n-doped semiconductor QD's, in which an electron resides in the conduction band of the n-doped semiconductor. In this paper, we choose an electron effective mass $m = 0.063m_0$ corresponding to n-doped GaAs QD's, where $m_0 = 9.109\,3826 \times 10^{-31}$ kg is the rest mass of electrons. $d_{0z} = -(16/9\pi^2)eL$, $e = 1.602 \times 10^{-19}$ C, and $\hbar = 1.054 \times 10^{-34}$ J s. For example, when ω_A corresponds to the wavelength $\lambda_A = 1.5$ μm, $L = 4.652$ nm and $|d_{0z}| = 1.342 \times 10^{-28}$ C m. The breakdown field of GaAs is $E = 4.0 \times 10^7$ V/m. In what follows, for the sake of numerical simplicity, we use SiO$_2$ and GaN in 1D and 2D PC's, respectively. The breakdown fields of SiO$_2$ and GaN are $E = 5.0 \times 10^8$ and 1.0×10^8 V/m, respectively.

III. NUMERICAL RESULTS AND DISCUSSION

A. One-dimensional photonic crystal with a quantum-dot layer

As a diagnostic of our self-consistent Maxwell-Bloch model, we consider a simplified 1D photonic crystal. We consider a hypothetical 1D model PC composed of SiO$_2$ layers in the air. [See Fig. 1(a).] Dielectric constants of SiO$_2$ and air are $\epsilon = 2.25$ and $\epsilon = 1$, respectively. A thickness of the SiO$_2$ layers is $d/a = 0.2$, where a is the lattice constant. We assume that $\omega a/2\pi c = a/\lambda = 0.403$ corresponds to $\lambda = 1.5$ μm, obtained by choosing $a = 604.5$ nm. Figure 1(b) shows the photonic band structure calculated with 31 plane waves by the PWE method, exhibiting the first and second PBG's as $0.4080 \leqslant \omega a/2\pi c \leqslant 0.4959$ and $0.8524 \leqslant \omega a/2\pi c \leqslant 0.9673$, respectively. We consider 21 SiO$_2$ layers: For $|x - la| \leqslant d/2$ (with integer $|l| \leqslant 10$), $\epsilon = 2.25$; otherwise, $\epsilon = 1.0$. Figure 1(c) shows the LDOS's at $x/a = 0.0$ and $|x|/a = 0.5$ calculated by Eq. (38). Blue solid and red dashed lines indicate the LDOS's at $x/a = 0.0$ and $|x|/a = 0.5$, respectively. Fabry-Perot-type oscillations in the LDOS's result from the finite nature of the structures. As shown in Fig. 1, LDOS's strongly depend on positions. We focus on LDOS's near the first PBG. While the LDOS at $x/a = 0.0$ (blue solid line) is strongly enhanced near the upper edge of the first photonic band due to the high field concentration in the high dielectric component, the LDOS at $|x|/a = 0.5$ (red dashed line) is strongly enhanced near the lower edge of the second photonic band, where field intensity concentrates in the low dielectric region. In what follows, we assume that a QD layer is distributed at $x/a = 0.0$ and that electric fields are polarized in the z direction. Since the QD region L is small enough, the influence of the QD layer on the 1D LDOS can be neglected. A single QD occupies the area $L \times L$ in the yz direction. We consider two kinds of areal densities of QD's in the yz plane at $x/a = 0.0$. One is the case that a single QD is distributed per area $3L \times 3L$, and then, $N_A = 1/(3L \times 3L)$. The other is the case that a single QD is distributed per area $L \times L$, and then, $N_A = 1/(L \times L)$. While this would imply that QD's in a single layer are closely packed, an equivalent physical realization (leading to the same effective dipole coupling strength) corresponds to multiple layers of QD's at $x/a = 0.0$. We neglect the transfer of electrons to neighboring QD's. For $L = 4.652$ nm ($\lambda_A = 1.5$ μm), $N_A = 1/(3L \times 3L)$ and $1/(L \times L)$ are 5.134×10^{15} and 4.621×10^{16} dots/m^2, respectively. These high areal densities of InAs QD's have already been fabricated experimentally [32,33].

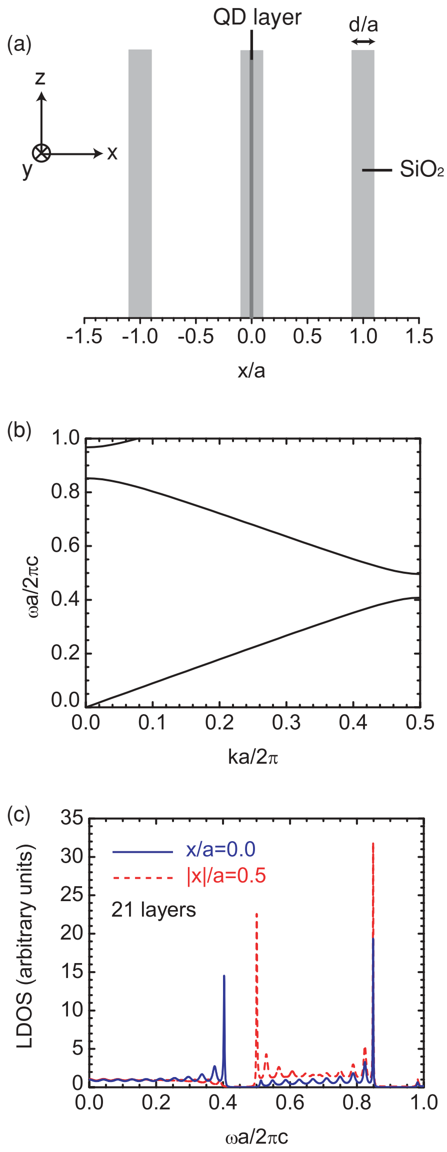

FIG. 1. (Color online) (a) Idealized 1D PC structure with 1D LDOS jumps. Dielectric constants of SiO$_2$ and air are $\epsilon = 2.25$ and $\epsilon = 1$, respectively. The thickness of SiO$_2$ layers is $d/a = 0.2$, where $a = 604.5$ nm is the lattice constant. (b) Photonic band structure for infinite 1D PC's. First and second PBG's occur at $0.4080 \leqslant \omega a/2\pi c \leqslant 0.4959$ and $0.8524 \leqslant \omega a/2\pi c \leqslant 0.9673$, respectively. (c) LDOS's at $x/a = 0.0$ and $|x|/a = 0.5$ calculated by Eq. (38) for a finite-size 21-layer stack. Blue solid and red dashed lines indicate the LDOS's at $x/a = 0.0$ and $|x|/a = 0.5$, respectively.

1. Semiclassical simulation of spontaneous radiative emission

In this section we verify that our semiclassical Maxwell Bloch equations, including incident and radiated electromagnetic fields, recaptures the phenomenon of radiative spontaneous emission without recourse to any phenomenological

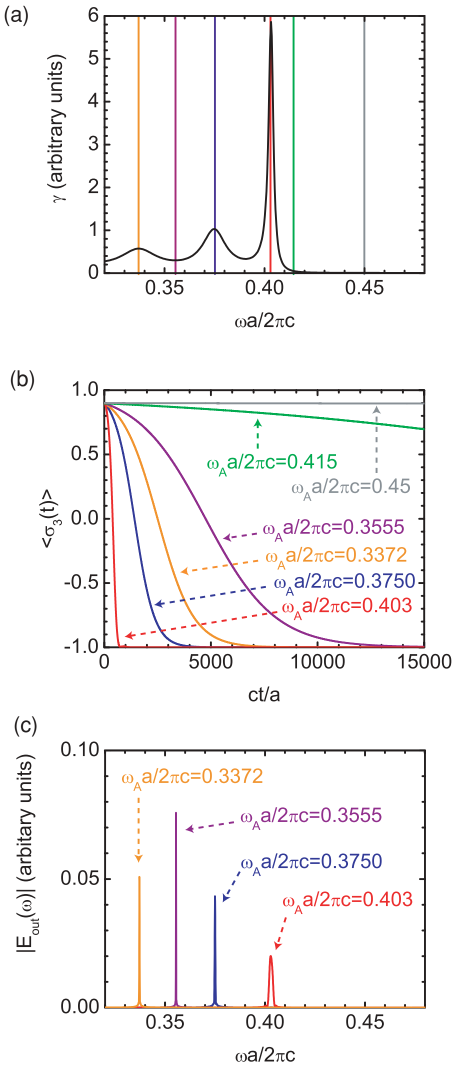

FIG. 2. (Color online) (a) Spontaneous emission rate γ evaluated by FDTD at $x/a = 0.0$ in 21-layer 1D PC stack of Fig. 1. $\omega_A a/2\pi c = 0.3372$, 0.3555, 0.375, 0.403, 0.415, and 0.45 are focused. (b) QD population $\langle\sigma_3(t)\rangle$ as a function of time for weak coupling $N_A = 1/(3L \times 3L)$. Multiplying ct/a by $a/c = 2.015 \times 10^{-3}$ ps gives real time. (c) Fourier spectrum of the emitted electric fields at $\omega_A a/2\pi c = 0.3372$, 0.3555, 0.3750, and 0.403 for $N_A = 1/(3L \times 3L)$.

decay parameters. Our formulation describes both weak- and strong-coupling effects.

The radiative spontaneous emission rate γ from an excited QD is proportional to the transition frequency and the LDOS [$\gamma \propto \omega\rho_{\mathrm{LDOS}}(\omega)$] [12–14]. First, we consider $N_A = 1/(3L \times 3L)$. Figure 2(a) shows the spontaneous emission rate at $x/a = 0.0$. This γ is calculated by multiplying the LDOS in Fig. 1(c) by ω. We neglect phonon dephasing and consider a test of our self-consistent Maxwell-Bloch equation to describe spontaneous emission. In our semiclassical model, we neglect quantum fluctuations in the electromagnetic vacuum. Therefore, it is necessary to trigger the radiative emission process by imposing a small initial polarization on the atom. At $ct/a = 0.0$, we set up $\langle\sigma_1(0)\rangle = \sqrt{1 - \langle\sigma_3(0)\rangle^2}\cos\theta$, $\langle\sigma_2(0)\rangle = \sqrt{1 - \langle\sigma_3(0)\rangle^2}\sin\theta$, and $\langle\sigma_3(0)\rangle = 0.9$ ($\langle\sigma_1(0)\rangle^2 + \langle\sigma_2(0)\rangle^2 + \langle\sigma_3(0)\rangle^2 = 1$). Since $\langle\sigma_3(t)\rangle$ does not depend on θ, we take $\theta = 0$. We focus on $\omega_A a/2\pi c = 0.3372$, 0.3555, 0.3750, 0.403, 0.415, and 0.45. Then, 4.402 nm ($\omega_A a/2\pi c = 0.45$) $\leqslant L \leqslant$ 5.086 nm ($\omega_A a/2\pi c = 0.3372$). Figure 2(b) shows the spontaneous emission dynamics of $\langle\sigma_3(t)\rangle$ as obtained by the self-consistent Maxwell-Bloch equation for $N_A = 1/(3L \times 3L)$. Multiplying ct/a by $a/c = 2.015 \times 10^{-3}$ ps gives real time. For example, $ct/a = 5000$ corresponds to $t = 10.075$ ps. As shown in Fig. 2(b), $\langle\sigma_3(t)\rangle$ rapidly decays near the photonic band edge at $\omega_A a/2\pi c = 0.403$. On the other hand, $\langle\sigma_3(t)\rangle$ is almost constant within the PBG at $\omega_A a/2\pi c = 0.45$. Orders of fast spontaneous emission are $\omega_A a/2\pi c = 0.403$, 0.3750, 0.3372, 0.3555, 0.415, and 0.45. These results coincide with magnitudes of γ in Fig. 2(a). We detect emitted electric fields outside the PC's and Fourier transform them with respect to time. Then, we obtain the Fourier spectrum of the output electric fields $|E_{\mathrm{out}}(\omega)| = |\int_0^\infty dt e^{i\omega t} E_{\mathrm{out}}(t)|$. Figure 2(c) shows the Fourier spectrum of the emitted electric fields at $\omega_A a/2\pi c = 0.3372$, 0.3555, 0.3750, and 0.403 in the case of $N_A = 1/(3L \times 3L)$. These frequency components have sharp peaks, and the width of the peaks increases with larger γ.

Despite the absence of any phenomenological decay parameter, we accurately recapture the spontaneous emission using our Maxwell-Bloch equations. In our model, time-dependent electric polarizations (dipoles) act as electric current densities [Eq. (32)], the electric current densities radiate electromagnetic fields (dipole radiation), and the dipole radiation causes the loss of electronic excitation energy. Therefore, $\langle\sigma_3(t)\rangle$ transfers to -1 (ground state).

Next, we consider $N_A = 1/(L \times L)$. This provides an effective strong-coupling regime between light and QD's. Figure 3(a) shows the spontaneous emission rate at $x/a = 0.0$ and is the same as Fig. 2(a). We focus on the same frequencies as in Fig. 2. Figure 3(b) shows the spontaneous emission of $\langle\sigma_3(t)\rangle$ as a function of time in the case of $N_A = 1/(L \times L)$. As shown in Figs. 2(b) and 3(b), the decay time in the case of $N_A = 1/(L \times L)$ is faster than that in the case of $N_A = 1/(3L \times 3L)$. For example, when focusing on $\omega_A a/2\pi c = 0.3555$ in Figs. 2(b) and 3(b), $\langle\sigma_3(t)\rangle$ become mostly -1 at $ct/a = 13\,500$ (27.2025 ps) and 1600 (3.224 ps), respectively. This is because dipole radiation is proportional to N_A, as shown in Eqs. (32) and (33). In Fig. 3(b), moreover, $\langle\sigma_3(t)\rangle$ at $\omega_A a/2\pi c = 0.403$ decays with oscillations suggesting coherent feedback and memory effects, unlike in Fig. 2(b). Figure 3(c) shows the Fourier spectrum of the emitted electric fields at $\omega_A a/2\pi c = 0.3372$, 0.3555, 0.3750, and 0.403 in the case of $N_A = 1/(L \times L)$. Peaks in Fig. 3(c) become broader than those in Fig. 2(c) due to strong coupling. It should be noted that in Fig. 3(c) the Fourier spectrum at $\omega_A a/2\pi c = 0.403$ has two peaks. This phenomenon is called vacuum Rabi splitting [34]. The large LDOS at $\omega_A a/2\pi c = 0.403$ enhances electromagnetic fields, and the large N_A provides a large effective transition dipole. This Rabi splitting occurs when the interaction of QD's and emitted electric fields is very strong. This clearly demonstrates that our Maxwell-Bloch equations recapture important effects relevant to QD switching in a structured electromagnetic vacuum, as described in subsequent sections of this paper.

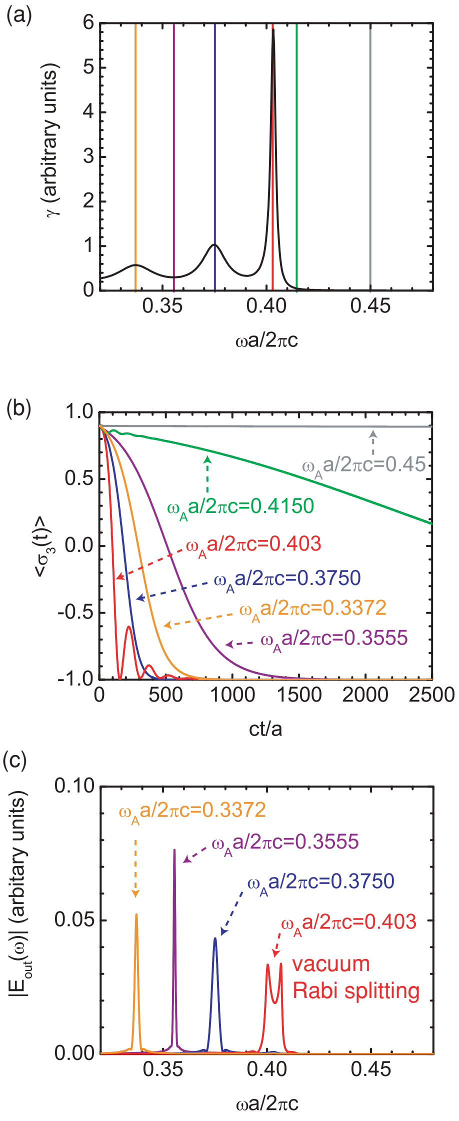

FIG. 3. (Color online) (a) Spontaneous emission rate γ at $x/a = 0.0$ for 21-layer 1D stack. We focus on $\omega_A a/2\pi c = 0.3372$, 0.3555, 0.375, 0.403, 0.415, and 0.45. (b) QD population $\langle\sigma_3(t)\rangle$ as a function of time for $N_A = 1/(L \times L)$. Multiplying ct/a by $a/c = 2.015 \times 10^{-3}$ ps gives real time. (c) Fourier spectrum of the emitted electric fields at $\omega_A a/2\pi c = 0.3372$, 0.3555, 0.3750, and 0.403 in the case of $N_A = 1/(L \times L)$. Vacuum Rabi splitting is apparent at 1D band edge.

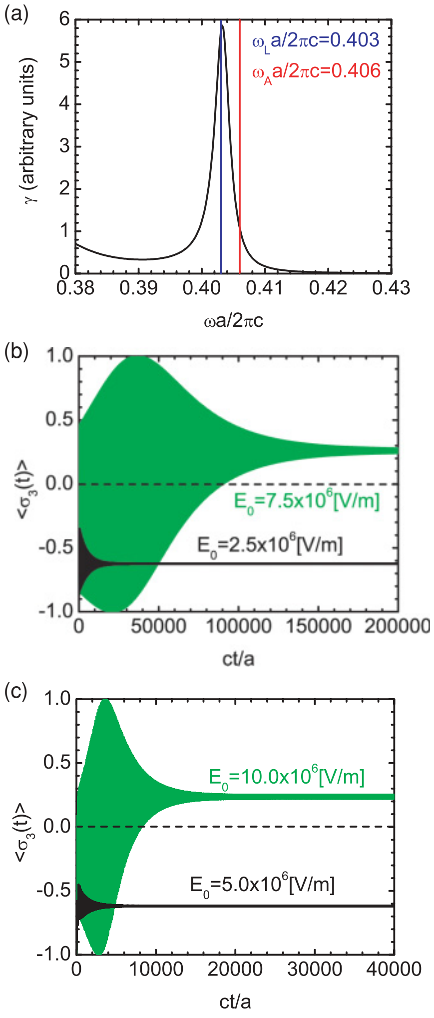

FIG. 4. (Color online) (a) Laser and atomic frequencies $\omega_L a/2\pi c = 0.403$ and $\omega_A a/2\pi c = 0.406$ ($\Delta_{AL} a/2\pi c = 0.003 > 0$) relative to the spontaneous emission band edge peak for 21-layer 1D PC stack. (b) Temporal behavior of $\langle\sigma_3(t)\rangle$ driven by continuous-wave optical field for weak coupling $N_A = 1/(3L \times 3L)$. $E_0 = 2.5 \times 10^6$ V/m and 7.5×10^6 V/m are considered. (c) Temporal behavior of $\langle\sigma_3(t)\rangle$ driven by continuous-wave optical field for strong coupling $N_A = 1/(L \times L)$. $E_0 = 5.0 \times 10^6$ V/m and 1.0×10^7 V/m are considered. Rapid radiative relaxation leads faster steady-state saturation.

2. *Population inversion driven by continuous waves*

We now consider QD population inversion driven by continuous electric fields polarized in the z direction. We start with no phonon dephasing. At $ct/a = 0.0$, we set $\langle\sigma_1(0)\rangle = 0.0$, $\langle\sigma_2(0)\rangle = 0.0$, and $\langle\sigma_3(0)\rangle = -1.0$. The external electric field $\mathbf{E}_{\text{in}} = \boldsymbol{\varepsilon}(e^{i\omega_L t} + e^{-i\omega_L t})$ with the laser frequency ω_L causes $\langle\sigma_3(t)\rangle$ to oscillate with the Rabi frequency 2Ω, where $2\Omega = \sqrt{(2\mathbf{d}_0 \cdot \boldsymbol{\varepsilon}/\hbar)^2 + \Delta_{AL}^2}$ and $\Delta_{AL} = \omega_A - \omega_L$. This leads to three frequency components, ω_L and $\omega_L \pm 2\Omega$ (Mollow triplet), in the radiative electromagnetic fields [17]. We refer to the spontaneous emission rates at $\omega_L - 2\Omega$ and $\omega_L + 2\Omega$ as γ_- and γ_+, respectively. In previous studies [12,13], it was shown that the steady-state $\langle\sigma_3(t)\rangle$ becomes $\langle\sigma_3\rangle^{\text{st}} = (\Delta_{AL}/2\Omega)[(\gamma_- s^4 - \gamma_+ c^4)/(\gamma_- s^4 + \gamma_+ c^4)]$, where $s^2 = (1/2)[1 - (\Delta_{AL}/2\Omega)]$ and $c^2 = (1/2)[1 + (\Delta_{AL}/2\Omega)]$. To obtain population inversion ($\langle\sigma_3\rangle^{\text{st}} > 0$), we require either the conditions $\Delta_{AL} > 0$ and $\gamma_-/\gamma_+ > c^4/s^4 > 1$ or $\Delta_{AL} < 0$ and $\gamma_+/\gamma_- > s^4/c^4 > 1$ to be satisfied. We choose the former condition. Figure 4(a) shows the laser and atomic frequencies $\omega_L a/2\pi c = 0.403$ and $\omega_A a/2\pi c = 0.406$ ($\Delta_{AL} a/2\pi c = 0.003 > 0$) in relation to the spontaneous emission peak caused by the 1D photonic band edge. Then, $(\omega_L - 2\Omega)a/2\pi c \leqslant 0.400$ and $(\omega_L + 2\Omega)a/2\pi c \geqslant 0.406$. $\langle\sigma_3\rangle^{\text{st}}$ becomes positive when electric fields exceed the threshold value. $E_{\text{in}}(t) = E_0 \sin \omega_L t$ is input from the left side of the 1D PC.

Figure 4(b) shows the behavior of $\langle\sigma_3(t)\rangle$ driven by continuous waves as a function of time in the case of $N_A = 1/(3L \times 3L)$. $\langle\sigma_3(t)\rangle$ converges to a steady-state value

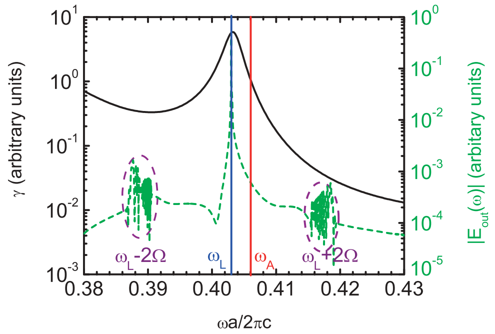

FIG. 5. (Color online) Fourier spectrum (green dashed line) of emitted radiation showing Mollow components at ω_L and $\omega_L \pm 2\Omega$ for $E_0 = 1.0 \times 10^7$ V/m in Fig. 4(c) relative to band-edge spontaneous emission peak (black solid line). $\omega_L \pm 2\Omega$ are highlighted by purple dashed circles.

with diminishing Rabi oscillations 2Ω. While $\langle\sigma_3(t)\rangle^{\text{st}}$ at $E_0 = 2.5 \times 10^6$ V/m is negative, $\langle\sigma_3\rangle^{\text{st}}$ at $E_0 = 7.5 \times 10^6$ V/m is positive. On the other hand, while the saturation time at $E_0 = 2.5 \times 10^6$ V/m is $ct/a \simeq 20\,000$ (40.3 ps), the saturation time at $E_0 = 7.5 \times 10^6$ V/m is $ct/a \simeq 200\,000$ (403.0 ps).

More rapid saturation of population inversion is achieved with strong coupling. Figure 4(c) shows the behavior of $\langle\sigma_3(t)\rangle$ driven by continuous waves as a function of time in the case of $N_A = 1/(L \times L)$. While $\langle\sigma_3\rangle^{\text{st}}$ at $E_0 = 5.0 \times 10^6$ V/m is negative, $\langle\sigma_3\rangle^{\text{st}}$ at $E_0 = 10 \times 10^6$ V/m is positive. On the other hand, while the saturation time at $E_0 = 5.0 \times 10^6$ V/m is $ct/a \simeq 4000$ (8.06 ps), the saturation time at $E_0 = 10 \times 10^6$ V/m is $ct/a \simeq 20\,000$ (40.3 ps). Therefore, strong coupling of QD's to the electromagnetic field is useful for rapid saturation of population inversion. This, in turn, facilitates high-speed all-optical information processing with QD's in PC's.

We next investigate signatures of the Mollow triplet when population inversion occurs. We detect the output electric fields on the right side of the 1D PC and Fourier transform them with respect to time. Figure 5 shows the Fourier spectrum (green dashed line) of the output electric fields at $E_0 = 10 \times 10^6$ V/m in Fig. 4(c). $\omega_L \pm 2\Omega$ are highlighted by purple dashed circles. When $(\omega_L - 2\Omega)a/2\pi c = 0.3880$ and $(\omega_L + 2\Omega)a/2\pi c = 0.4180$ $(2\Omega a/2\pi c = 0.015)$, the ratio of corresponding spontaneous emission rates becomes $\gamma_-/\gamma_+ \simeq 0.3502/0.0330 = 10.61$. Remarkably, population inversion is achieved, even with a relatively modest jump in the electromagnetic LDOS.

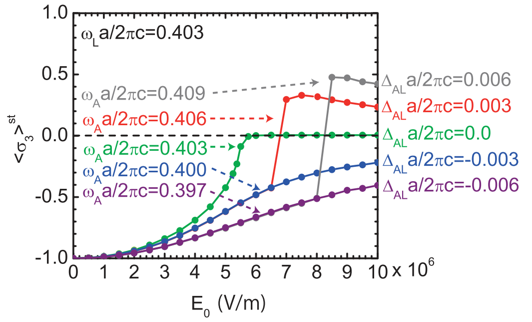

FIG. 6. (Color online) Steady-state values of $\langle\sigma_3(t)\rangle$ as a function of continuous-wave field strength E_0 for various atomic frequencies in the strong-coupling case of $N_A = 1/(L \times L)$. For $\omega_L a/2\pi c = 0.403$, $\omega_A a/2\pi c = 0.397$, 0.400, 0.403, 0.406, and 0.409 are considered. Population switching occurs for positive dephasing $\Delta_{AL} > 0$.

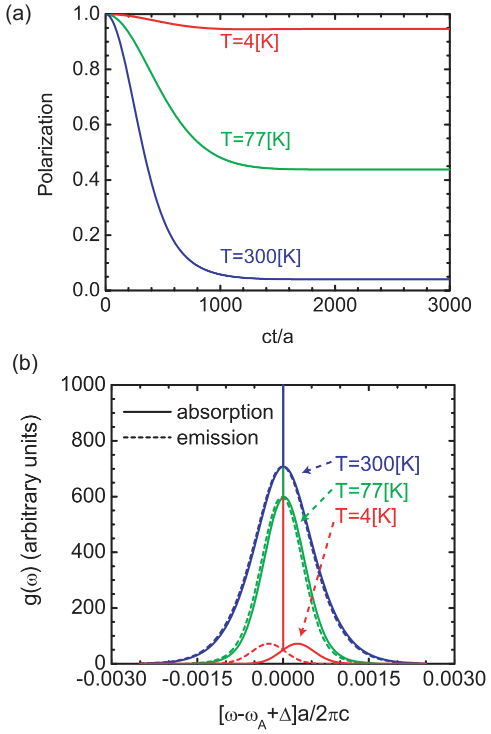

FIG. 7. (Color online) (a) Behavior of atomic polarization $|e^{-i(\omega_A-\Delta)t}e^{R(\pm t)-S}|$ with undamped phonons for the δ-pulse electric field as a function of time and (b) absorption (solid line) and emission (dashed line) line shapes of QD's in Eq. (13), respectively, for various temperatures such as $T = 4$, 77, and 300 K. We choose acoustic phonon wave-vector cutoff $L = 4.953$ nm $(\omega_A a/2\pi c = 0.3555)$.

In Fig. 6, we show the saturated $\langle\sigma_3(t)\rangle$ as a function of E_0 for various atomic frequencies in the case of $N_A = 1/(L \times L)$. At $\omega_L a/2\pi c = 0.403$, we consider $\omega_A a/2\pi c = 0.397$, 0.400, 0.403, 0.406, and 0.409. When $\omega_A a/2\pi c = 0.397$ and 0.400, $\langle\sigma_3\rangle^{\text{st}}$ monotonically increases as a function of E_0 but always remains negative. When $\omega_A a/2\pi c = 0.403$, $\langle\sigma_3\rangle^{\text{st}}$ is mostly zero after it monotonically increases as a function of E_0. However, when $\omega_A a/2\pi c = 0.406$ and 0.409, $\langle\sigma_3\rangle^{\text{st}}$ becomes positive when E_0 exceeds a threshold value. For these two cases, the behaviors of $\langle\sigma_3\rangle^{\text{st}}$ at $\omega_A a/2\pi c = 0.406$ and 0.409 are the same as those at $\omega_A a/2\pi c = 0.400$ and 0.397, respectively, below the threshold values. While at $\omega_A a/2\pi c = 0.406$ there is a threshold value between $E_0 = 6.5 \times 10^6$ and 7.0×10^6 V/m, at $\omega_A a/2\pi c = 0.409$ the threshold occurs between $E_0 = 8.0 \times 10^6$ and 8.5×10^6 V/m. In summary, when $\Delta_{AL} > 0$, we obtain population inversion driven by continuous waves. The steady-state inversion $\langle\sigma_3\rangle^{\text{st}}$ and the threshold value increase with larger Δ_{AL}.

3. *Influence of phonon dephasing*

First, we consider the effects of phonon dephasing on QD switching and inversion with undamped phonons. In Fig. 7(a), we show the polarization behavior of $|e^{-i(\omega_A-\Delta)t}e^{R(\pm t)-S}|$ for the δ-pulse electric field $\mathbf{E}(t) = \mathbf{E}_0\delta(t)$ as a function of

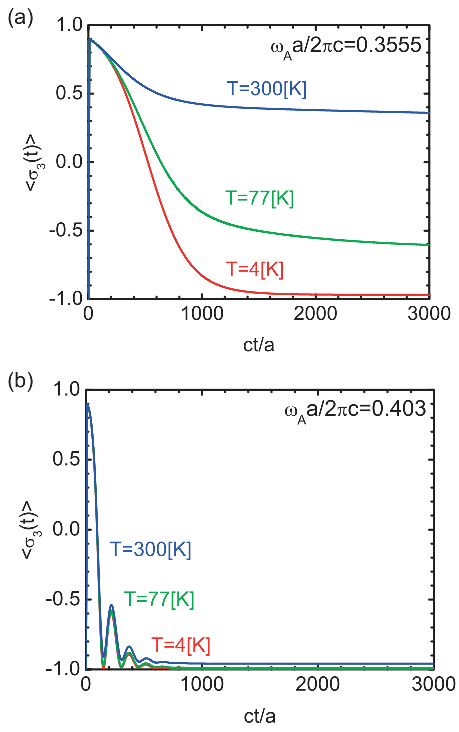

FIG. 8. (Color online) Spontaneous emission of $\langle\sigma_3(t)\rangle$ at $\omega_A a/2\pi c =$ (a) 0.3555 and (b) 0.403 as a function of time for various temperatures in the case of $N_A = 1/(L \times L)$ due to phonon dephasing with undamped phonons. $T = 4, 77$, and 300 K are considered.

time in the absence of spontaneous emission, as discussed in Sec. II A 2. Figure 7(b) depicts the absorption and emission line shapes of QD's in Eq. (13) for various temperatures, such as $T = 4, 77$, and 300 K. In the case of longitudinal acoustic phonons, $\eta_{\mathbf{q}} = \sqrt{\hbar q/2\rho c_l L^3}(D_2 - D_1)\exp(-q^2L^2/4)$ and $\omega_{\mathbf{q}} = c_l q$, where D_1 and D_2 are the deformation potentials of the ground and excited states, respectively. In GaAs, $\rho = 5370$ kg/m^3, $c_l = 5110$ m/s, and $D_2 - D_1 = -9.8$ eV. For example, we choose $L = 4.953$ nm ($\omega_A a/2\pi c = 0.3555$). In Fig. 7(a), the polarizations decay faster with higher temperature and are saturated near $ct/a = 1500$ (3.023 ps), which is the phonon dephasing time. In Fig. 7(b), the absorption (solid line) and emission (dashed line) line shapes of QD's have sharp peaks at $\omega = \omega_A - \Delta$ and become broader with higher temperature. Moreover, the absorption and emission line shapes show broad peaks in higher- and lower-frequency regions, respectively, arising from multiple phonon absorption and emission side bands. However, this difference of the absorption and emission line shapes becomes smaller with increasing temperature.

In Figs. 8(a) and 8(b), we show the spontaneous emission dynamics of $\langle\sigma_3(t)\rangle$ at $\omega_A a/2\pi c = 0.3555$ (where LDOS is low) and 0.403 (where LDOS is large), respectively, as a function of time for various temperatures in the case of $N_A = 1/(L \times L)$, including the effects of phonon dephasing with undamped phonons. $T = 4, 77$, and 300 K are considered. At $ct/a = 0.0$, we set up $\langle\sigma_3(0)\rangle = -1$, apply a hypothetical strong electric field $E = 1.0 \times 10^8 \sin[(\omega_A - \Delta)t]$ V/m at the QD layer until $\langle\sigma_3(t)\rangle = 0.9$, and then turn off the field. In Fig. 8(a), $\langle\sigma_3(t)\rangle$ decays rapidly as the polaronic cloud forms around the QD until $ct/a = 1500$ (3.023 ps). After $ct/a = 1500$ (3.023 ps), the decay of $\langle\sigma_3(t)\rangle$ proceeds very slowly due to the dephasing of the transition dipole by the phonon cloud and reduction of the effective transition matrix element due to the Frank-Condon reduction of the overlap between the excited-state and ground-state wave functions. In the absence of phonon damping, this leads to the unusual artifact that spontaneous emission decay is slower at high temperatures compared to lower temperatures. At high temperatures, there are more phonons available to contribute to the Frank-Condon effect. However, as we show below, phonon damping significantly restricts the Frank-Condon reduction of the transition dipole matrix element. In Fig. 8(b), we consider spontaneous emission in a high LDOS spectral range, and $\langle\sigma_3(t)\rangle$ does not vary much with temperature. This is because the radiative time scale $ct/a = 800$ (1.612 ps) of $\langle\sigma_3(t)\rangle$ at $\omega_A = 0.403$ is shorter than the phonon dephasing time $ct/a = 1500$ (3.023 ps). In other words, when the spontaneous emission timescale with no phonon dephasing is shorter than the phonon dephasing time, the radiative relaxation is insensitive to temperature.

In practice, however, we must consider the phonon dephasing with damped phonons. For simplicity, the phonon decay rate is considered constant $\gamma_{\mathbf{q}} = \gamma_{\text{ph}}$. A more realistic model for phonon lifetime due to lattice anharmonicity and the breakup of high-frequency phonons into lower-energy phonons can be found elsewhere [30,35,36]. Typically, this leads to a damping rate that is proportional to the phonon frequency and strongly temperature dependent. We focus on $\omega_A a/2\pi c = 0.3555$. In Fig. 9(a), we show the polarization behavior of $|e^{-i(\omega_A - \bar{\Delta})t - \Gamma_{\text{damp}}t}e^{\bar{R}(\pm t) - \bar{S}(\pm t)}|$ for the δ-pulse electric field $\mathbf{E}(t) = \mathbf{E}_0\delta(t)$ as a function of time in the absence of spontaneous emission, as discussed in Sec. II A 3. Figure 9(b) depicts the absorption and emission line shapes of QD's in Eq. (22) at $T = 77$ K. $\gamma_{\text{ph}}a/c = 0.0$ and 2.0×10^{-4} are considered. $\gamma_{\text{ph}}a/c = 2.0 \times 10^{-4}$ ($\gamma_{\text{ph}}^{-1} = 10.075$ ps) corresponds to $\Gamma_{\text{damp}}a/c = 1.468 \times 10^{-4}$ ($\Gamma_{\text{damp}}^{-1} = 13.72$ ps). In experiments, the relaxation time of electromagnetic fields radiated from excited InGaAs QD's at $T = 75$ K is 11 ps [37], which is close to $\Gamma_{\text{damp}}^{-1}$. In Fig. 9(a), while the polarization for $\gamma_{\text{ph}}a/c = 0.0$ retains a nonzero value, on the timescale under consideration, the polarization for $\gamma_{\text{ph}}a/c = 2.0 \times 10^{-4}$ decays more rapidly to zero. In Fig. 9(b), the absorption (solid line) and emission (dashed line) line shapes become broader, and the peak becomes lower with increasing γ_{ph}. Figure 9(c) shows the spontaneous emission for $\gamma_{\text{ph}}a/c = 0.0$ and 2.0×10^{-4} at $T = 77$ K in the case of $N_L = 1/(L \times L)$. For $\gamma_{\text{ph}}a/c = 2.0 \times 10^{-4}$, we consider $\Gamma_{\text{pop}} = \Gamma_{\text{damp}}/10$ (dashed line) and $\Gamma_{\text{pop}} = \Gamma_{\text{damp}}$ (solid line). In the case of damped phonons, Γ_{damp} makes the dipole radiation finish faster than in the case of undamped phonons. After that, however, $\langle\sigma_3(t)\rangle$ decays monotonically due to Γ_{pop}. While for $\Gamma_{\text{pop}} = \Gamma_{\text{damp}}/10$ $\langle\sigma_3(t)\rangle$ decays slowly, for $\Gamma_{\text{pop}} = \Gamma_{\text{damp}}$ it converges to -1 relatively quickly. This is quite distinct from the case of undamped phonons where the excited state is artificially preserved by a polaronic cloud that displaces the excited-state wave function from the ground state for long times. In the case of damped phonons, with increasing temperature, while radiative decays decrease, nonradiative decays increase.

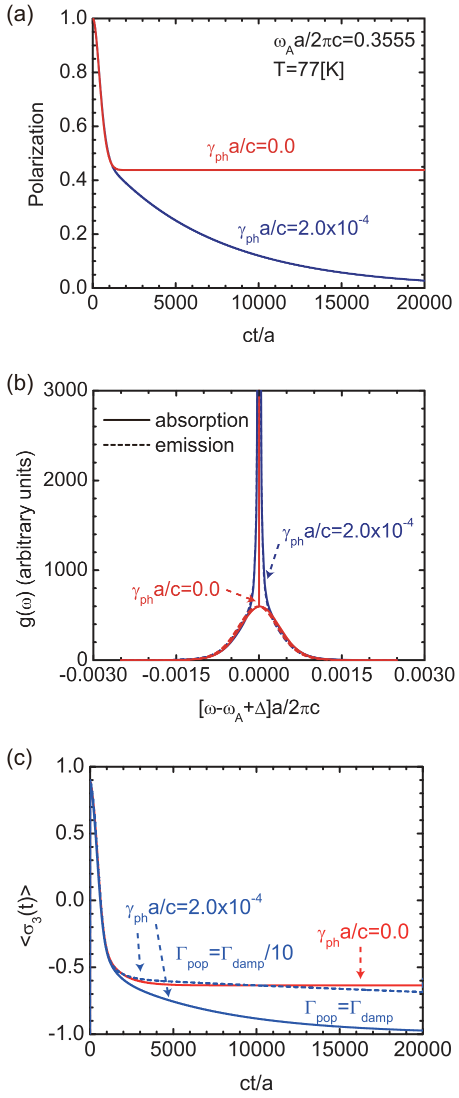

FIG. 9. (Color online) (a) Behavior of atomic polarization $|e^{-i(\omega_A-\bar{\Delta})t-\Gamma_{\rm damp}t}e^{\bar{R}(\pm t)-\bar{S}}|$ with damped phonons for the δ-pulse electric filed as a function of time and (b) absorption (solid line) and emission (dashed line) lineshapes of QD's for $\gamma_{ph}a/c = 0.0$ and 2.0×10^{-4} at $T = 77$ K. $\gamma_{ph}a/c = 0.0$ and 2.0×10^{-4} are considered. (c) Spontaneous emission for $\gamma_{ph}a/c = 0.0$ and 2.0×10^{-4} at $T = 77$ K in the case of $N_L = 1/(L \times L)$. Dashed and solid lines indicate $\Gamma_{\rm pop} = \Gamma_{\rm damp}/10$ and $\Gamma_{\rm pop} = \Gamma_{\rm damp}$, respectively. We focus on $\omega_A a/2\pi c = 0.3555$.

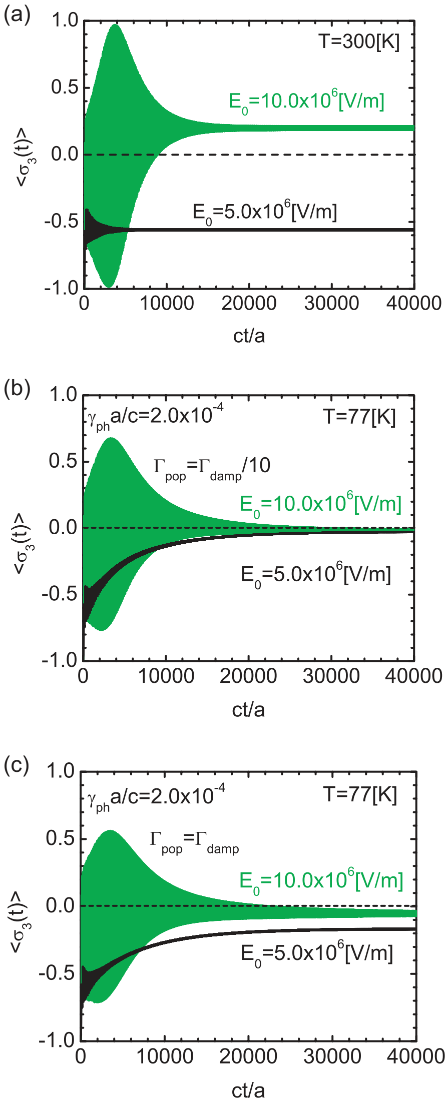

FIG. 10. (Color online) (a) Behavior of $\langle\sigma_3(t)\rangle$ driven by continuous waves as a function of time at $T = 300$ K in the case of $N_A = 1/(L \times L)$ due to phonon dephasing with undamped phonons. Laser and atomic frequencies are $\omega_L a/2\pi c = 0.403$ and $\omega_A a/2\pi c = 0.406$, respectively. (b) and (c) Behaviors of $\langle\sigma_3(t)\rangle$ driven by continuous waves as a function of time at $T = 77$ K for $\gamma_{ph}a/c = 2.0 \times 10^{-4}$ and $\Gamma_{\rm pop} = \Gamma_{\rm damp}/10$ and $\Gamma_{\rm pop} = \Gamma_{\rm damp}$, respectively, in the case of $N_A = 1/(L \times L)$ due to phonon dephasing with damped phonons.

Figure 10(a) shows the behaviors of $\langle\sigma_3(t)\rangle$ driven by continuous waves as a function of time at $T = 300$ K in the case of $N_A = 1/(L \times L)$ with dephasing by undamped phonons. Laser and atomic frequencies are $\omega_L a/2\pi c = 0.403$ and $\omega_A a/2\pi c = 0.406$, respectively. Behaviors of $\langle\sigma_3(t)\rangle$ in Fig. 10 are slightly distorted compared to Fig. 4(c). (Maximum and minimum amplitudes of $\langle\sigma_3(t)\rangle$ do not reach 1 and -1, respectively.) While the saturated $\langle\sigma_3(t)\rangle$ at $E_0 = 5.0 \times 10^6$ V/m increases with temperature, that at $E_0 = 10.0 \times 10^6$ V/m decreases with temperature. Nevertheless, the temperature dependence of behaviors of $\langle\sigma_3(t)\rangle$ is relatively small since the time period of Rabi oscillations $1/[2\Omega a/2\pi c] = 66.667$ (0.1343 ps) in Fig. 5 is much shorter than the phonon dephasing time $ct/a = 1500$ (3.023 ps). On the other hand, Fig. 10(b) shows the behaviors of $\langle\sigma_3(t)\rangle$ driven by continuous waves as a function of time at $T = 77$ K for $\gamma_{\rm ph}a/c = 2.0 \times 10^{-4}$ and $\Gamma_{\rm pop} = \Gamma_{\rm damp}/10$ in the case of $N_A = 1/(L \times L)$ with dephasing by damped phonons. $\langle\sigma_3(t)\rangle$ at both $E_0 = 5 \times 10^6$ V/m and 10×10^6 V/m converge to almost the same negative value. Likewise, Fig. 10(c) shows the behaviors of $\langle\sigma_3(t)\rangle$ driven by continuous waves as a function of time at $T = 77$ K for $\gamma_{\rm ph}a/c = 2.0 \times 10^{-4}$ and $\Gamma_{\rm pop} = \Gamma_{\rm damp}$ in the case of $N_A = 1/(L \times L)$. The saturated $\langle\sigma_3(t)\rangle$ at $E_0 = 5 \times 10^6$ and 10×10^6 V/m are lifted. Clearly, the damped phonons hinder QD population inversion.

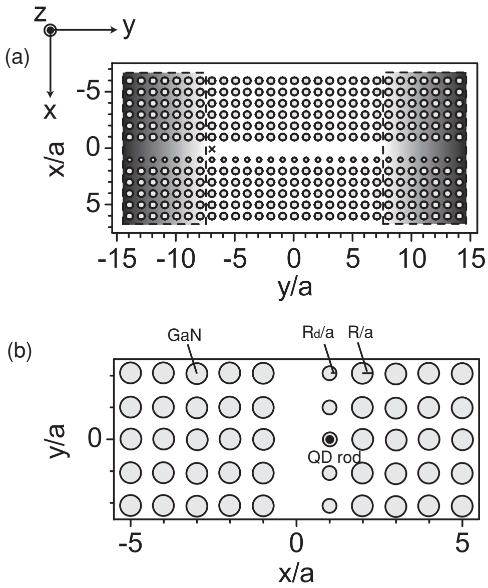

FIG. 11. (a) Bimodal waveguides in a 2D PC composed of GaN circular rods in the air. The dielectric constant of GaN is $\epsilon = 5.3$, and a radius of rods is $R/a = 0.3$ ($a = 564$ nm). Two adjacent rows are composed of air and dielectric rods with smaller radii $R_d/a = 0.2$. In the FDTD method, the computational region is $|x|/a \leqslant 7.5$ and $|y|/a \leqslant 15.5$. (b) Structure for $|x|/a \leqslant 5.5$ and $|y/a| \leqslant 2.5$. A QD rod is placed at $(x/a, y/a) = (1.0, 0.0)$.

B. Quantum-dot response in a bimodal 2D photonic crystal waveguide

We now consider a PC geometry closer to those discussed for on-chip control of light flow [19]. Here the electromagnetic LDOS experiences a sudden jump throughout the length of a bimodal waveguide channel as the result of a cutoff in one of the two waveguide modes. We consider a QD with transition frequency near this LDOS jump. In Fig. 11(a), we show the bimodal waveguide in the 2D PC's composed of GaN circular rods in the air. In the 2D PC's, a dielectric constant of GaN is $\epsilon = 5.3$, and the radius of rods is $R/a = 0.3$, where a is the lattice constant. Two adjacent rows of rods conduct light in an air waveguide mode (no rods) and dielectric waveguide mode (with rods smaller radii $R_d/a = 0.2$). We assume that $\omega a/2\pi c = a/\lambda = 0.376$ corresponds to the wavelength $\lambda = 1.5$ μm, and then, $a = 564$ nm. In the FDTD method, we take the computational region for $|x|/a \leqslant 7.5$ and $|y|/a \leqslant 15.5$. A cross symbol at $(x/a, y/a) = (0.0, -7.0)$ indicates the source point of light. In this case, we need the light propagation without reflections in the air waveguide. For this purpose, tapered waveguides, in which entrance and exit become gradually wider, are widely used [38,39]. For computational simplicity, however, we impose the gradual conductivity near the ends of the waveguide segment with $\sigma(x,y)a/\epsilon_0 c = 3[(|y|/a - 7.5)/7.0]^2$ for $|x|/a \leqslant 6.5$, $|y|/a \geqslant 7.5$, and $|y|/a \leqslant 14.5$ highlighted by dashed boxes. Otherwise, in the interior of the system, $\sigma(x,y) = 0.0$. Under this condition, the light near $\omega a/2\pi c = 0.376$ can propagate without reflections. For $|y|/a \leqslant 7.5$, there is no absorption (conductivity). Figure 11(b) shows the structure for $|x|/a \leqslant 5.5$ and $|y|/a \leqslant 2.5$. A QD rod is placed at $(x/a, y/a) = (1.0, 0.0)$.

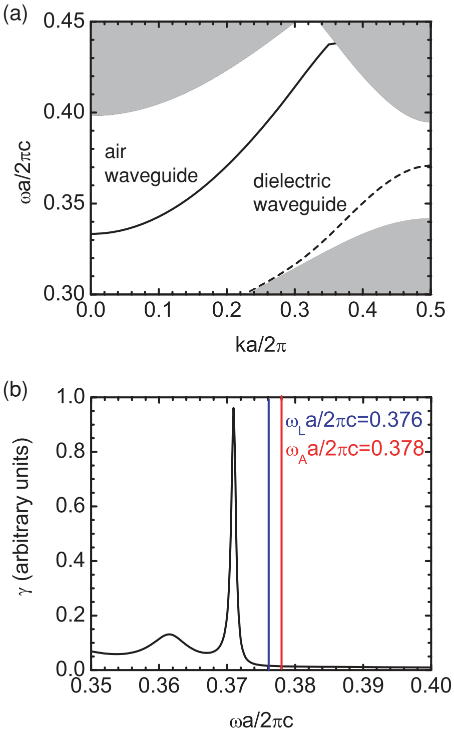

FIG. 12. (Color online) (a) The 2D TM guided modes for bimodal waveguide in Fig. 11. Solid and dashed lines indicate the guided modes localized near air and dielectric regions, respectively. Shaded regions indicate the photonic bands projected to the y direction. In the dashed line, there is a cutoff frequency inside the PBG, although there are no cutoff frequencies in the solid line inside the PBG. (b) Spontaneous emission rate at $(x/a, y/a) = (1.0, 0.0)$. Laser and atomic frequencies are $\omega_L a/2\pi c = 0.376$ and $\omega_A a/2\pi c = 0.378$, respectively.

We consider the 2D TM mode with electric fields polarized in the z direction. In Fig. 12(a), we show the 2D TM guided modes of Fig. 11 calculated with 1661 plane waves by the PWE method. For this calculation, a supercell is taken for $|x|/a \leqslant 7.5$ and $|y|/a \leqslant 0.5$. Solid and dashed lines indicate the guided modes localized near air and dielectric waveguides, respectively. Shaded regions indicate the photonic bands projected to the y direction. In the dielectric waveguide dispersion, there is a cutoff frequency inside the PBG. In the air-waveguide dispersion there is no cutoff inside the PBG. Figure 12(b) shows the spontaneous emission rate at $(x/a, y/a) = (1.0, 0.0)$. The spontaneous emission rate is greatly enhanced near $\omega a/2\pi c = 0.371$ since the photonic band edge associated with the dielectric mode cutoff in Fig. 12(a) provides a large electromagnetic density of states. While the air waveguide is used for inputting light, the dielectric waveguide is used to embed the QD rod possessing the abrupt change of γ. When light propagates in the air waveguide, the electric field is maximum at $x/a = 0.0$ (main peak). The electric field also has side peaks near $|x|/a = 1.0$ when the row of small dielectric rods resides. We excite the QD rod through the side peak near $x/a = 1.0$. Laser and atomic

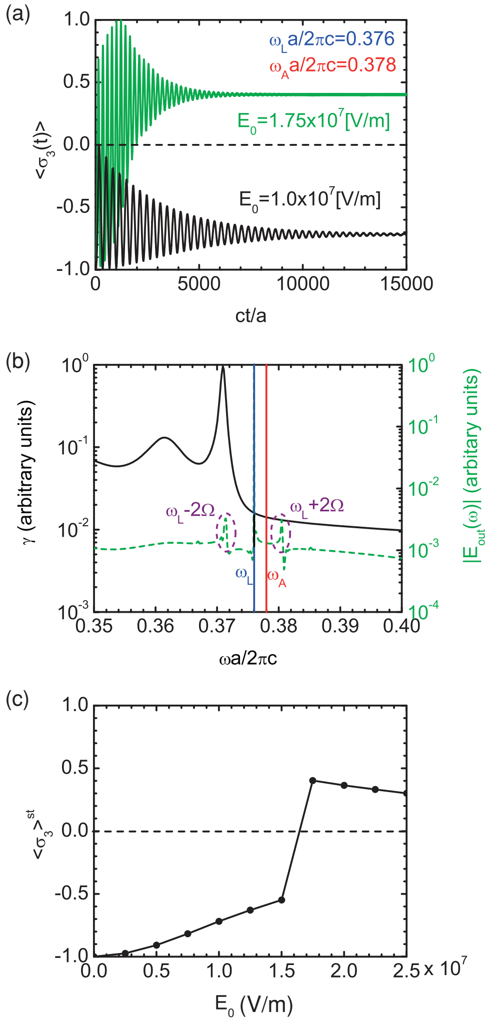

FIG. 13. (Color online) (a) Behavior of $\langle\sigma_3(t)\rangle$ driven by continuous waves as a function of time in the case of $N_L = 5 \times 5/L$. $E_0 = 1.0 \times 10^7$ and 1.75×10^7 V/m are considered. Multiplying ct/a by $a/c = 1.88 \times 10^{-3}$ ps gives real time. (b) Fourier spectrum (green dashed line) of the output electric fields for $E_0 = 1.75 \times 10^7$ V/m in (a). $\omega_L \pm 2\Omega$ are highlighted by purple dashed circles. Spontaneous emission is depicted in black. (c) Saturated $\langle\sigma_3(t)\rangle$ as a function of E_0 in the case of $N_L = 5 \times 5/L$.

frequencies are $\omega_L a/2\pi c = 0.376$ and $\omega_A a/2\pi c = 0.378$, respectively.

1. Population inversion driven by continuous waves

As discussed in Sec. III A 2, a QD rod with high coupling strength at $(x/a,y/a) = (1.0,0.0)$ is necessary for a short saturation time of $\langle\sigma_3(t)\rangle$. When the length of a single QD is $L = 4.640$ nm ($\omega_A a/2\pi c = 0.378$), we assume that 5×5 QD's are distributed near $(x/a,y/a) = (1.0,0.0)$ in the 2D xy plane and that these QD's are close packed in the z direction with no vertical spacing between QD's. We neglect any transfer of electrons between QD's. Then, the linear density of the QD rod is $N_L = 5 \times 5/L = 5.388 \times 10^9$ dots/m. In a real, physical 3D system this choice in 2D can be regarded as simply a device for simulating strong coupling. In 3D waveguide systems, this may appear as a strongly enhanced local electromagnetic density of states (Purcell factor) [16,20]. It could also arise from collective response of many QD's experiencing the same optical field. Since the area that these QD's occupy is approximately 25 nm × 25 nm in the 2D xy plane, the influence of the QD rod on the 2D LDOS can be neglected.

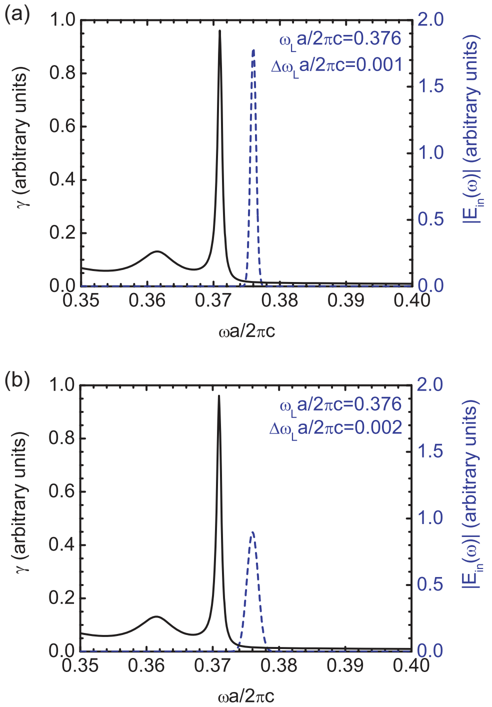

FIG. 14. (Color online) Fourier spectrum of input pulse $E_{\rm in}(t)$ in the case of (a) $\Delta\omega_L a/2\pi c = 0.001$ ($cT/a = 2000$) and (b) 0.002 ($cT/a = 1000$). Black solid and blue dashed lines indicate the spontaneous emission rate and the Fourier spectrum, respectively. The Fourier spectrum is a Gaussian function with center frequency $\omega_L a/2\pi c = 0.376$.

At $(x/a,y/a) = (0.0,-7.0)$ in Fig. 11(a), we excite $E_{\rm in}(t) = E_0 \sin\omega_L t$, where E_0 is the steady-state maximum amplitude of the main peak at $(x/a,y/a) = (0.0,0.0)$ when there are no QD rods in PC's. In the FDTD method, then, the steady-state maximum amplitude of the side peak at $(x/a,y/a) = (1.0,0.0)$ is approximately $0.63E_0$. We consider no phonon dephasing. At $ct/a = 0.0$, we set up $\langle\sigma_1(0)\rangle = 0.0$, $\langle\sigma_2(0)\rangle = 0.0$, and $\langle\sigma_3(0)\rangle = -1.0$. Figure 13(a) shows the behaviors of $\langle\sigma_3(t)\rangle$ driven by continuous waves as a function of time in the case of $N_L = 5 \times 5/L$. Multiplying ct/a by $a/c = 1.88 \times 10^{-3}$ ps gives real time. For example, $ct/a = 5000$ corresponds to $t = 9.40$ ps. While $\langle\sigma_3\rangle^{\rm st}$ at $E_0 = 1.0 \times 10^7$ V/m is negative, $\langle\sigma_3\rangle^{\rm st}$ at $E_0 = 1.75 \times 10^7$ V/m is positive. While the saturation time at $E_0 = 1.0 \times 10^7$ V/m is $ct/a \simeq 15\,000$ (28.2 ps), the saturation time at $E_0 = 1.75 \times 10^7$ V/m is $ct/a \simeq 8000$ (15.04 ps). These time scales can be made shorter in structures that support a high electromagnetic LDOS than that considered in our idealized 2D model systems. We investigate the Mollow triplet by detecting output electric fields at $(x/a,y/a) = (0.0,0.0)$ and Fourier transforming them with respect to time. Figure 13(b) shows the Fourier spectrum (green dashed line) of the output electric fields at $E_0 =$

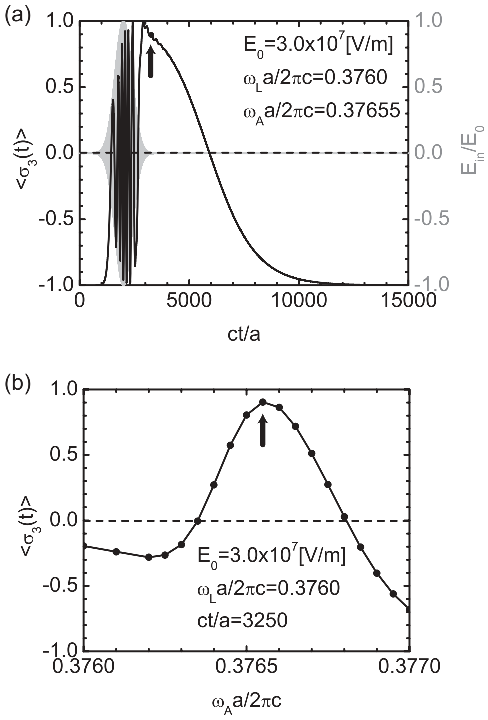

FIG. 15. (a) Behavior of $\langle\sigma_3(t)\rangle$ driven by a pulse with $\Delta\omega_L a/2\pi c = 0.001$ as a function of time in the case of $N_L = 5 \times 5/L$. The atomic frequency is $\omega_A a/2\pi c = 0.37655$. Shaded regions indicate the time pulse. An arrow indicates the value of $\langle\sigma_3(t)\rangle$ at $ct/a = 3250$. (b) Behavior of $\langle\sigma_3(t)\rangle$ at $ct/a = 3250$ as a function of atomic frequencies in the case of $N_L = 5 \times 5/L$. An arrow indicates $\langle\sigma_3(t)\rangle$ in (a).

1.75×10^7 V/m in Fig. 13(a). $\omega_L \pm 2\Omega$ are highlighted by purple dashed circles. When $(\omega_L - 2\Omega)a/2\pi c = 0.3715$ and $(\omega_L + 2\Omega)a/2\pi c = 0.3805$ ($2\Omega a/2\pi c = 0.0045$), $\gamma_-/\gamma_+ \simeq 0.3221/0.01303 = 24.72$. Although this contrast is not as high as considered previously [15,16], population inversion is, nevertheless, achieved. In Fig. 13(c), we show the saturated $\langle\sigma_3(t)\rangle$ as a function of E_0 in the case of $N_L = 5 \times 5/L$. $\langle\sigma_3\rangle^{\mathrm{st}}$ becomes positive when E_0 exceeds the threshold value, after it monotonically increases with E_0 under the threshold value. The threshold occurs between $E_0 = 1.5 \times 10^7$ V/m and $E_0 = 1.75 \times 10^7$ V/m.

2. Population inversion driven by optical pulses

We now consider population inversion driven by pulses composed of the superposition of frequency components. To input the pulses without distortion, these frequency components should have nearly the same group velocities. As shown in Fig. 12(a), the dispersion relation of the air waveguide is mostly linear near $\omega_L a/2\pi c = 0.376$. In Fig. 11(a), therefore, we can input the pulses with the center frequency $\omega_L a/2\pi c = 0.376$ without distortion.

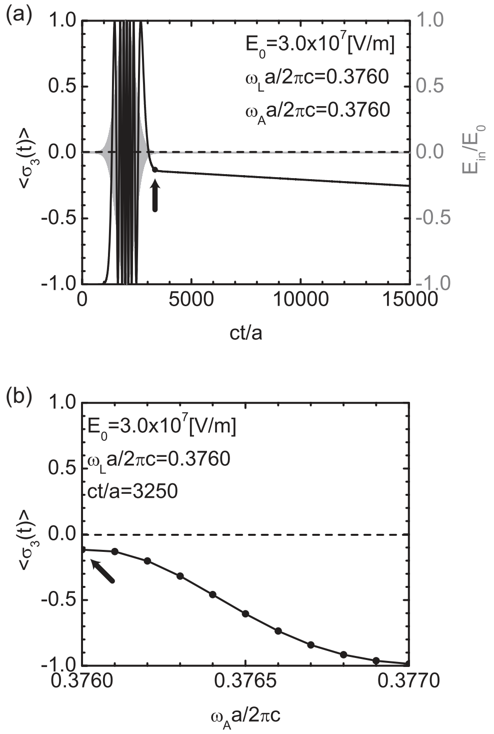

FIG. 16. (a) Behavior of $\langle\sigma_3(t)\rangle$ driven by a pulse with $\Delta\omega_L a/2\pi c = 0.001$ as a function of time in the case of $N_L = 1/(2L)$. The atomic frequency is $\omega_A a/2\pi c = 0.3760$. Shaded regions indicate the temporal pulse. An arrow indicates the value of $\langle\sigma_3(t)\rangle$ at $ct/a = 3250$. (b) Behavior of $\langle\sigma_3(t)\rangle$ at $ct/a = 3250$ as a function of atomic frequencies in the case of $N_L = 1/(2L)$. An arrow indicates the $\langle\sigma_3(t)\rangle$ in (a).

At $(x/a, y/a) = (0.0, -7.0)$ in Fig. 11(a), we excite $E_{\mathrm{in}}(t) = E_0 e^{-\alpha(t-T)^2} \sin\omega_L t$ [$\alpha = (\pi/\sqrt{\ln 2}T)^2$ and $cT/a = 2/(\Delta\omega_L a/2\pi c)$], where E_0 is the maximum amplitude of the main peak at $(x/a, y/a) = (0.0, 0.0)$ when there are no QD rods in PC's. In what follows, we fix $\omega_L a/2\pi c = 0.376$ and $E_0 = 3.0 \times 10^7$ V/m. $\Delta\omega_L$ is the full width at half maximum (FWHM) of the Fourier spectrum $|E_{\mathrm{in}}(\omega)| = |\int_0^\infty dt e^{i\omega t} E_{\mathrm{in}}(t)|$. Then, $E_{\mathrm{in}}(t)$ has the FWHM $c\Delta t_L/a = (2\ln 2/\pi)(cT/a)$. In Figs. 14(a) and 14(b), we show the Fourier spectrum of $E_{\mathrm{in}}(t)$ in the case of $\Delta\omega_L a/2\pi c = 0.001$ [$cT/a = 2000$ and $c\Delta t_L/a = 882.54$ (1.66 ps)] and 0.002 [$cT/a = 1000$ and $c\Delta t_L/a = 441.27$ (0.83 ps)], respectively. Black solid and blue dashed lines indicate the spontaneous emission rate and the Fourier spectrum, respectively. The Fourier spectrum is a Gaussian function with center frequency $\omega_L a/2\pi c = 0.376$. Although the maximum value of the Fourier spectrum in Fig. 14(b) is smaller than that in Fig. 14(a), the Fourier spectrum in Fig. 14(b) is wider than that in Fig. 14(a). As shown later, the time pulse in Fig. 14(b) is shorter than that in Fig. 14(a). These two pulses can propagate in the air waveguide without reflections or distortions. As a first illustration, we neglect phonon dephasing. At $ct/a = 0.0$, we set up $\langle\sigma_1(0)\rangle = 0.0$, $\langle\sigma_2(0)\rangle = 0.0$, and $\langle\sigma_3(0)\rangle = -1.0$.

First, we consider an optical pulse with $\Delta\omega_L a/2\pi c = 0.001$ ($cT/a = 2000$) in Fig. 14(a). The FWHM of the pulse is $c\Delta t_L/a = 882.54$ (1.66 ps). It becomes nearly zero by $ct/a = (13/8)(cT/a) = 3250$. Figure 15(a) shows the behavior of $\langle\sigma_3(t)\rangle$ driven by a pulse with $\Delta\omega_L a/2\pi c = 0.001$ as a function of time in the case of $N_L = 5 \times 5/L$. The atomic frequency is $\omega_A a/2\pi c = 0.37655$. Shaded regions indicate the temporal profile of the pulse. $\langle\sigma_3(t)\rangle$ oscillates when the time pulse interacts with the QD rod. After the pulse passes, large population inversion $\langle\sigma_3(t)\rangle \simeq 1$ can be achieved. An

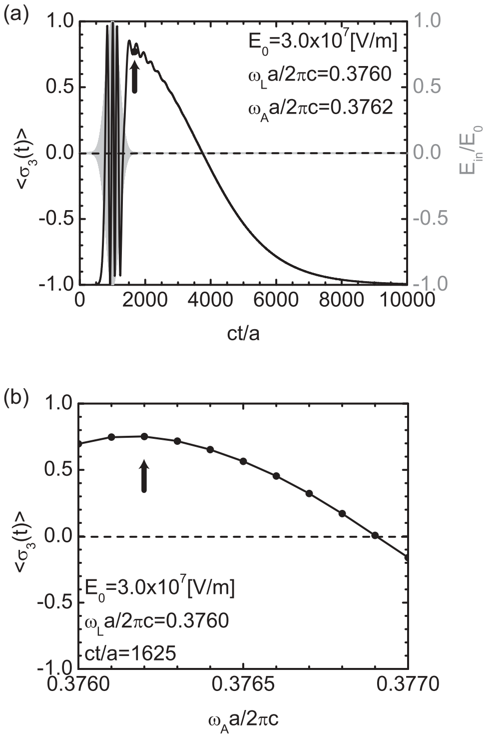

FIG. 17. (a) Behavior of $\langle\sigma_3(t)\rangle$ driven by a pulse with $\Delta\omega_L a/2\pi c = 0.002$ as a function of time in the case of $N_L = 5 \times 5/L$. The atomic frequency is $\omega_A a/2\pi c = 0.3762$. Shaded regions indicate the temporal pulse. An arrow indicates the value of $\langle\sigma_3(t)\rangle$ at $ct/a = 1625$. (b) Behavior of $\langle\sigma_3(t)\rangle$ at $ct/a = 1625$ as a function of atomic frequencies in the case of $N_L = 5 \times 5/L$. An arrow indicates the $\langle\sigma_3(t)\rangle$ in (a).

arrow indicates the $\langle\sigma_3(t)\rangle$ at $ct/a = 3250$. Figure 15(b) shows the behavior of $\langle\sigma_3(t)\rangle$ at $ct/a = 3250$ (when the exciting pulse has subsided) as a function of atomic frequency detuning from the pulse center frequency in the case of $N_L = 5 \times 5/L$. An arrow indicates $\langle\sigma_3(t)\rangle$ in Fig. 15(a). $\langle\sigma_3(t)\rangle$ at $ct/a = 3250$ becomes positive for $0.3764 \leqslant \omega_A a/2\pi c \leqslant 0.3768$ and maximum near $\omega_A a/2\pi c = 0.376\,55$. Although population inversion can be driven by pulses, rapid radiative spontaneous emission in our specific LDOS model causes $\langle\sigma_3(t)\rangle$ to decay rapidly after the pulse subsides. This could be compensated by a rapid sequence of optical pulses separated by about 10 ps in this oversimplified model that neglects all effects of phonons. Alternatively, we could replace the idealized 2D architecture with a more realistic 3D PBG waveguide architecture in which the rate of radiative spontaneous emission is much slower in the low density of states regime [16,20].

For comparison purposes, we consider a weak-coupling situation. We assume that a QD rod is placed at $(x/a, y/a) = (1.0,0.0)$ with $N_L = 1/(2L)$. Figure 16(a) shows the behavior of $\langle\sigma_3(t)\rangle$ driven by pulses with $\Delta\omega_L a/2\pi c = 0.001$ as a function of time. The atomic frequency is $\omega_A a/2\pi c = 0.3760$. Shaded regions indicate the temporal pulse profile. $\langle\sigma_3(t)\rangle$ oscillates when the pulse interacts with the QD rod. After the pulse passes, population inversion is not achieved, although the spontaneous emission of $\langle\sigma_3(t)\rangle$ is very slow. Figure 16(b) shows the behavior of $\langle\sigma_3(t)\rangle$ at $ct/a = 3250$ as a function of atomic frequency. Although $\langle\sigma_3(t)\rangle$ becomes maximum near $\omega_A a/2\pi c = 0.3760$, it always remains negative for $0.376 \leqslant \omega_A a/2\pi c \leqslant 0.377$. We show below that in order to achieve inversion with this weak coupling, a shorter pulse duration is required.

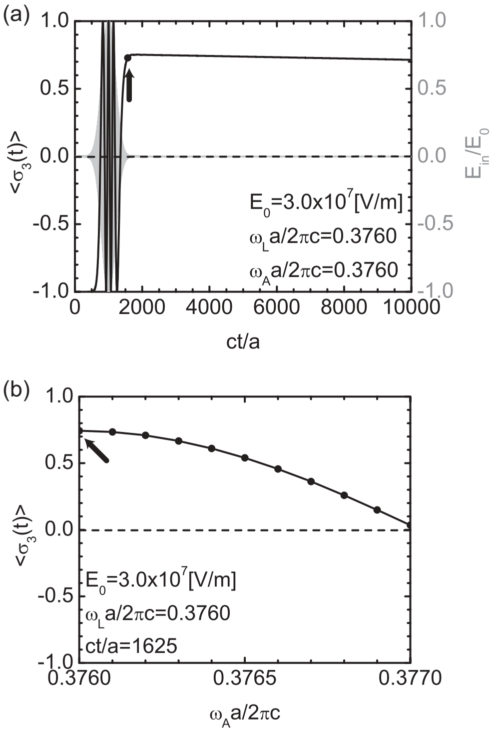

FIG. 18. (a) Behavior of $\langle\sigma_3(t)\rangle$ driven by a pulse with $\Delta\omega_L a/2\pi c = 0.002$ as a function of time in the case of $N_L = 1/(2L)$. The atomic frequency is $\omega_A a/2\pi c = 0.3760$. Shaded regions indicate the temporal pulse. An arrow indicates $\langle\sigma_3(t)\rangle$ at $ct/a = 1625$. (b) Behavior of $\langle\sigma_3(t)\rangle$ at $ct/a = 1625$ as a function of atomic frequencies in the case of $N_L = 1/(2L)$. An arrow indicates the $\langle\sigma_3(t)\rangle$ in (a).

We consider a short optical pulse with $\Delta\omega_L a/2\pi c = 0.002$ $(cT/a = 1000)$ and strong coupling in Fig. 14(b). The FWHM of the time pulse is $c\Delta t_L/a = 441.27$ (0.83 ps). This pulse is nearly zero by $ct/a = (13/8)(cT/a) = 1625$. Figure 17(a) shows the temporal behavior of $\langle\sigma_3(t)\rangle$, driven by this shorter pulse for $N_L = 5 \times 5/L$. The atomic frequency is $\omega_A a/2\pi c = 0.3762$. Shaded regions indicate the temporal pulse profile. $\langle\sigma_3(t)\rangle$ oscillates during the pulse interaction with the QD rod. After the pulse subsides, population inversion is achieved. Figure 17(b) shows the behavior of $\langle\sigma_3(t)\rangle$ at $ct/a = 1625$ as a function of atomic frequency. $\langle\sigma_3(t)\rangle$ at $ct/a = 1625$ becomes maximum near $\omega_A a/2\pi c = 0.3762$, and $\langle\sigma_3(t)\rangle$ is positive for $0.376 \leqslant \omega_A a/2\pi c \leqslant 0.3769$. Although population inversion can be driven by short pulses, the rapid spontaneous emission due to strong coupling and the absence of damped phonon-mediated dephasing in the specific LDOS model renders the switching effect short-lived.

Figure 18(a) shows the behaviors of $\langle\sigma_3(t)\rangle$ driven by a short pulse with $\Delta\omega_L a/2\pi c = 0.002$ in the weak-coupling case of $N_L = 1/(2L)$. The atomic frequency is $\omega_A a/2\pi c = 0.3760$. Shaded regions indicate the temporal pulse profile. $\langle\sigma_3(t)\rangle$ oscillates as the time pulse interacts with the QD rod. After a pulse subsides, population inversion $\langle\sigma_3(t)\rangle$ is achieved.

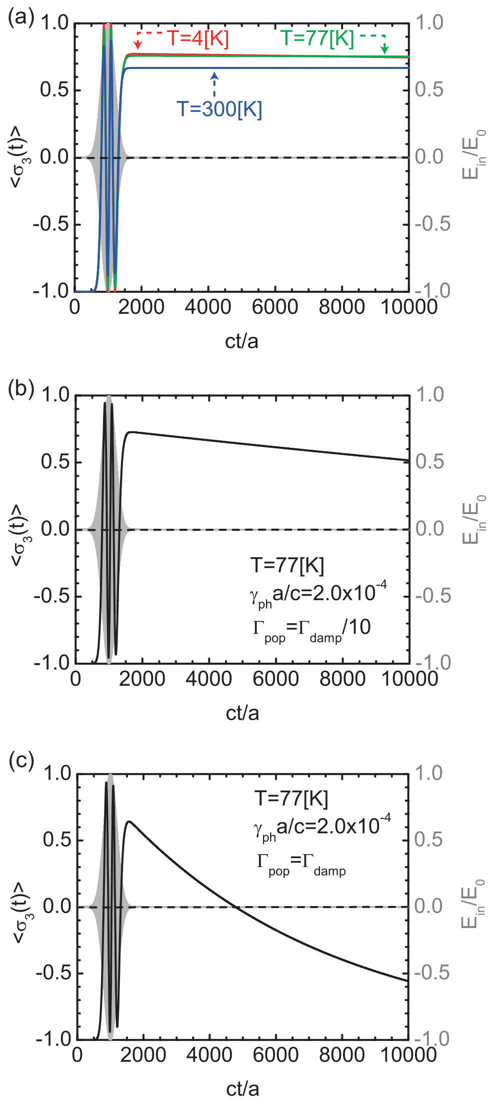

FIG. 19. (Color online) (a) Behavior of $\langle\sigma_3(t)\rangle$ driven by a pulse with $\Delta\omega_L a/2\pi c = 0.002$ as a function of time for various temperatures in the case of $N_L = 1/(2L)$ including phonon dephasing with undamped phonons. The atomic frequency is $\omega_A a/2\pi c = 0.3760$. $T = 4$, 77, and 300 K are considered. (b) and (c) Behaviors of $\langle\sigma_3(t)\rangle$ driven by a pulse with $\Delta\omega_L a/2\pi c = 0.002$ as a function of time at $T = 77$ K for $\gamma_{\rm ph} a/c = 2.0 \times 10^{-4}$ and $\Gamma_{\rm pop} = \Gamma_{\rm damp}/10$ and $\Gamma_{\rm pop} = \Gamma_{\rm damp}$, respectively, in the case of $N_L = 1/(2L)$ including phonon dephasing with damped phonons.

Figure 18(b) shows the behavior of $\langle\sigma_3(t)\rangle$ at $ct/a = 1625$ as a function of atomic frequencies in the case of $N_L = 1/(2L)$. $\langle\sigma_3(t)\rangle$ at $ct/a = 1625$ becomes maximum near $\omega_A a/2\pi c = 0.3760$, and $\langle\sigma_3(t)\rangle$ is always positive for $0.376 \leqslant \omega_A a/2\pi c \leqslant 0.377$. In this case of a shorter pulse and weaker coupling, the population inversion in Fig. 18(a) is preserved for a long time due to slow spontaneous emission from inverted state.

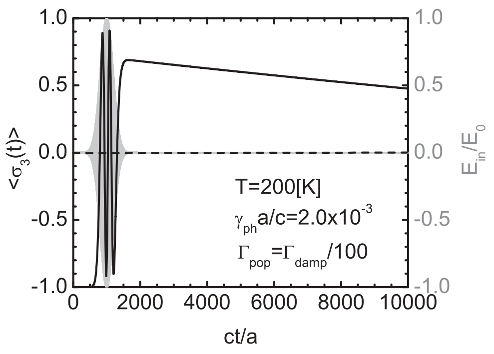

FIG. 20. Behavior of $\langle\sigma_3(t)\rangle$ driven by a pulse with $\Delta\omega_L a/2\pi c = 0.002$ including phonon dephasing with damped phonons as a function of time at $T = 200$ K for $\gamma_{\rm ph} a/c = 2.0 \times 10^{-3}$ and $\Gamma_{\rm pop} = \Gamma_{\rm damp}/100$ in the case of $N_L = 1/(2L)$.

We consider the influence of phonon dephasing with undamped phonons on $\langle\sigma_3(t)\rangle$ driven by pulses. Figure 19(a) shows the behavior of $\langle\sigma_3(t)\rangle$ driven by a short pulse with $\Delta\omega_L a/2\pi c = 0.002$ as a function of time for various temperatures in the weak-coupling case of $N_L = 1/(2L)$. In our model, the temperature simply sets the time scale of thermal phonon-mediated depolarization of the atomic dipole and the Frank-Condon reduction of the atomic transition dipole by the polaronic cloud. The atomic frequency is $\omega_A a/2\pi c = 0.3760$. Shaded regions indicate the optical pulse profile. After the pulse subsides, $\langle\sigma_3(t)\rangle$ at $T = 77$ K becomes larger than that at $T = 4$ K. However, $\langle\sigma_3(t)\rangle$ at $T = 300$ K is lower than those at $T = 4$ and 77 K. Nevertheless, at $T = 300$ K, we still obtain an effective population inversion. When the time period of Rabi oscillations is much shorter than the phonon dephasing time, the influence of phonon dephasing with undamped phonons is not so large.

Figure 19(b) shows the behavior of $\langle\sigma_3(t)\rangle$ driven by pulses with $\Delta\omega_L a/2\pi c = 0.002$ as a function of time at $T = 77$ K with phonon dephasing with damped phonons for $\gamma_{\rm ph} a/c = 2.0 \times 10^{-4}$ and $\Gamma_{\rm pop} = \Gamma_{\rm damp}/10$ ($\Gamma_{\rm damp}^{-1} = 12.03$ ps) in the case of $N_L = 1/(2L)$. Likewise, Fig. 19(c) shows the behavior of $\langle\sigma_3(t)\rangle$ driven by pulses with $\Delta\omega_L a/2\pi c = 0.002$ as a function of time at $T = 77$ K for $\gamma_{\rm ph} a/c = 2.0 \times 10^{-4}$ and $\Gamma_{\rm pop} = \Gamma_{\rm damp}$ in the case of $N_L = 1/(2L)$. Even in these cases, the effective population inversion can be obtained. However, for $\Gamma_{\rm pop} = \Gamma_{\rm damp}$, $\langle\sigma_3(t)\rangle$ decays rapidly.

Figure 20 shows the behavior of $\langle\sigma_3(t)\rangle$ driven by pulses with $\Delta\omega_L a/2\pi c = 0.002$ as a function of time at $T = 200$ K for $\gamma_{\rm ph} a/c = 2.0 \times 10^{-3}$ and $\Gamma_{\rm pop} = \Gamma_{\rm damp}/100$ ($\Gamma_{\rm damp}^{-1} = 1.16$ ps) in the case of $N_L = 1/(2L)$. Even in the case of rapid decay of polarizations, large population inversion can be obtained after the pulse subsides, provided that the Frank-Condon effect is capable of reducing the direct population decay rate.

C. Two-dimensional photonic-crystal waveguides with a side-coupled defect with a quantum-dot rod

Our QD inversion and switching behavior is not limited to waveguide cutoff geometries but also applies to other architectures with LDOS jumps. We consider an air waveguide with a side-coupled defect in 2D PC's composed of GaN rods with radii $R/a = 0.3$. The air waveguide is fabricated by removing one line of rods at $x/a = 0.0$, and the side-coupled defect has radius $R_d/a = 0.1$ and is located at $(x/a, y/a) = (2.0, 0.0)$. Figure 21(a) shows the spontaneous emission rate at the center of the side-coupled defect. The emission spectrum is maximum at $\omega a/2\pi c = 0.376$ and is broad since the

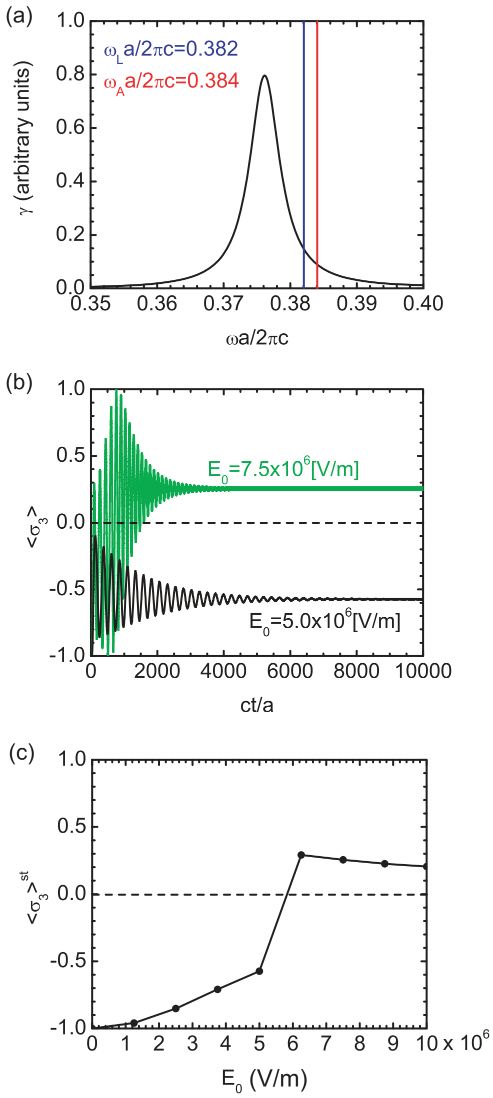

FIG. 21. (Color online) (a) Spontaneous emission rate at the center of the side-coupled defect. Laser and atomic frequencies are $\omega_L a/2\pi c = 0.382$ and $\omega_A a/2\pi c = 0.384$, respectively. (b) Behavior of $\langle\sigma_3(t)\rangle$ driven by a continuous wave as a function of time in the case of $N_L = 5 \times 5/L$. $E_0 = 5.0 \times 10^6$ and 7.5×10^6 V/m are considered. Multiplying ct/a by $a/c = 1.88 \times 10^{-3}$ ps gives real time. (c) Saturated $\langle\sigma_3(t)\rangle$ as a function of E_0 in the case of $N_L = 5 \times 5/L$.

side-coupled defect is near the air waveguide. A QD rod with the linear density of $N_L = 5 \times 5/L$ is distributed at the center of the side-coupled defect. We excite this strongly coupled QD rod by continuous waves. Laser and atomic frequencies are $\omega_L a/2\pi c = 0.382$ and $\omega_A a/2\pi c = 0.384$, respectively.

We input $E_{\text{in}}(t) = E_0 \sin \omega_L t$, where E_0 is the steady-state maximum amplitude at $(x/a, y/a) = (0.0, 0.0)$ of the air waveguide when there are no side-coupled defects. Figure 21(b) shows the behavior of $\langle\sigma_3(t)\rangle$ driven by continuous waves as a function of time in the strong-coupling case of $N_L = 5 \times 5/L$. We consider $E_0 = 5.0 \times 10^6$ and 7.5×10^6 V/m. Multiplying ct/a by $a/c = 1.88 \times 10^{-3}$ ps gives real time. For example, $ct/a = 5000$ corresponds to $t = 9.40$ ps. While $\langle\sigma_3\rangle^{\text{st}}$ at $E_0 = 5.0 \times 10^6$ V/m is negative, $\langle\sigma_3\rangle^{\text{st}}$ at $E_0 = 7.5 \times 10^6$ V/m is positive. While the saturation time at $E_0 = 5.0 \times 10^6$ V/m is $ct/a \simeq 10\,000$ (18.8 ps), the saturation time at $E_0 = 7.5 \times 10^6$ V/m is $ct/a \simeq 4000$ (7.52 ps). The pumping intensity required to achieve steady-state population inversion is lower than in Fig. 13(a) since electric fields are enhanced in the side-coupled defect.

In Fig. 21(c), we show the saturated $\langle\sigma_3(t)\rangle$ as a function of E_0 in the case of $N_L = 5 \times 5/L$. $\langle\sigma_3\rangle^{\text{st}}$ becomes positive when E_0 exceeds the threshold value, after it monotonically increases with E_0 under the threshold value. The inversion threshold occurs between $E_0 = 5.0 \times 10^6$ and $E_0 = 6.25 \times 10^6$ V/m

Finally, we consider switching and population inversion by short optical pulses for the side-coupled defect architecture. In this structure with $N_L = 1/(2L)$, however, population inversion cannot be achieved by time pulses of $E_0 = 1.0 \times 10^7$ V/m with $\Delta\omega_L a/2\pi c = 0.002$. In our numerical study, we fix the pulse center frequency $\omega_L a/2\pi c = 0.382$ and investigate the atomic frequency in the range $0.382 \leqslant \omega_A a/2\pi c \leqslant 0.383$. In this structure, large group velocity dispersion occurs near the resonant frequency of the side-coupled defect due to coupling of the defect and waveguide modes. Therefore, input pulses are spectrally and temporally distorted as they pass the QD region. Consequently, side-coupled defects are less suitable for population inversion and switching driven by short optical pulses.

IV. CONCLUSIONS

We have demonstrated population switching and inversion in 1D PC's and 2D PC waveguides using self-consistent Maxwell-Bloch equations. Stimulated emission and coherent feedback effects can be recaptured in this formulation. Spontaneous emission is also recaptured with no phenomenological decay terms, provided that small initial polarization to the atom is provided. The rate of spontaneous emission increases with coupling strength (larger areal density) of the QD layer. When the LDOS and the coupling strength are very large, Rabi splitting of the QD transition appears in the Fourier spectrum of the emitted electric field. Abrupt changes of LDOS's near photonic band edges enable population inversion driven by continuous waves. As a result of coherent feedback effects, the magnitude of this LDOS jump can be considerably less than previously anticipated [12–16,18,19]. Input electric fields must, nevertheless, exceed threshold values to obtain steady-state population inversion.

In our bimodal waveguide model, one mode has nearly linear dispersion inside the PBG, and the other guided mode has a frequency cutoff inside the PBG, leading to an abrupt change of the LDOS. These structures are appropriate for population inversion driven not only by continuous waves but also by pulses. Here pulses propagate without reflection or distortion. A short time pulse with the FWHM of 0.83 ps and peak electric field $E_0 = 3.0 \times 10^7$ V/m enables population inversion over a broad range of QD densities. However, lower QD densities enable long-term persistence of the population inversion after the exciting optical pulse has passed.

For side-coupled defects in 2D PC's, population inversion can be achieved by continuous waves. However, side-coupled defects are less suitable for population inversion driven by pulses due to pulse distortion effects as light enters and leaves the cavity mode directly from the waveguide mode. In the case of the bimodal waveguide channel, light is transferred between the linear dispersion mode and the vanishing group velocity mode by absorption and emission of light by the QD's. This process does not cause pulse distortion.

Phonon dephasing broadens the absorption and emission line shapes of the QD's. The phonon dephasing time with undamped phonons is approximately 3 ps. When the time scale of spontaneous emission and the time period of Rabi oscillations are shorter than the phonon dephasing time (with undamped phonons), the spontaneous emission and population inversion do not depend strongly on temperature. However, damped phonons provide a mechanism for nonradiative decay. Physically, this may arise from lattice anharmonicities leading to the breakup of individual phonons into two or more lower-energy phonons. This can lead to rapid deterioration of the QD inversion on the time scale of the phonon lifetime. On the other hand, this form of nonradiative decay is driven by the QD transition dipole. If dephasing effects and the Frank-Condon overlap effect rapidly diminish the atomic polarization and the effective transition dipole, the rate of atomic population decay may be slow compared to the damping rate of the atomic polarization. In this case, dynamic population switching of the QD may survive in the presence of phonon interactions.

In this paper, we have considered electric fields polarized in the z direction. Then, we can focus on two levels of the ground and excited states in QD's. Naturally, the Maxwell-Bloch equations can be extended to 2D TE modes and 3D PC's. However, in 2D TE modes in which electric fields are parallel to the 2D xy plane, there are two excited states for the electric fields polarized in the x and y directions. In other words, we must consider the nearly degenerate excited states in QD's [24]. In realistic 3D PC's, moreover, there may be three relevant excited states for the electric fields polarized in the x, y and z directions [26].

The most important outcome of our self-consistent Maxwell-Bloch theory is the ability to achieve dynamic switching and population inversion, with short optical pulses, using structures with considerably smaller jumps in the local electromagnetic density of states than previously anticipated. This is the result of coherent feedback and stimulated emission in the high LDOS region, which effectively enhances the ratio of emission rates between the QD Mollow components in the high and low LDOS regions. Consequently, population inversion may be possible in shorter waveguide segments in 3D PBG materials and in 2D membrane PC's where the LDOS ratios for a bimodal waveguide are smaller due to the background continuum of 3D optical modes. Coherent feedback from slow-group velocity modes also leads to memory effects in the QD, which influence the response of the QD to a sequence of optical pulse separated by short time intervals. In previous studies [15,16], the final inverted QD state achieved after passage of an optical pulse was nearly independent of initial state of the atomic Bloch vector. This was due to the rapid rate of radiative relaxation in the high LDOS region without coherent feedback. In our case, dephasing and nonradiative decay by coupling to damped phonons are required to erase the memory of the final Bloch vector (after the pulse passes) to the initial Bloch vector (prior to pulse arrival). These issues require more detailed consideration for the application of our dynamic switching effect to optical information processing by streams of optical pulses.

ACKNOWLEDGMENTS

This work was supported in part by the Natural Sciences and Engineering Research Council of Canada, the Canadian Institute for Advanced Research, and the Platinum Medal grant from the Premier of Ontario.

APPENDIX: POLARON TRANSFORMED ATOMIC POLARIZATION

Here we provide details of the derivation of Eq. (12). Using $\tilde{c}_1^\dagger(t) = \tilde{c}_1^\dagger(0) - i\int_0^t d\tau \frac{\mathbf{d_0}\cdot\mathbf{E}(\tau)}{\hbar}\tilde{c}_2^\dagger(\tau)D_+(\tau)$ and $\tilde{c}_2(t) = \tilde{c}_2(0)e^{-i(\omega_A-\Delta)t} + i\int_0^t d\tau e^{-i(\omega_A-\Delta)(t-\tau)}\frac{\mathbf{d_0}\cdot\mathbf{E}(\tau)}{\hbar}D_+(\tau)\tilde{c}_1(\tau)$,

$$\begin{aligned}\tilde{c}_1^\dagger(t)D_-(t)\tilde{c}_2(t) = {}& \tilde{c}_1^\dagger(0)D_-(t)\tilde{c}_2(0)e^{-i(\omega_A-\Delta)t} - i\int_0^t d\tau e^{-i(\omega_A-\Delta)t}\frac{\mathbf{d_0}\cdot\mathbf{E}(\tau)}{\hbar}\tilde{c}_2^\dagger(\tau)D_+(\tau)D_-(t)\tilde{c}_2(0)\\ &+i\int_0^t d\tau e^{-i(\omega_A-\Delta)(t-\tau)}\frac{\mathbf{d_0}\cdot\mathbf{E}(\tau)}{\hbar}\tilde{c}_1^\dagger(0)D_-(t)D_+(\tau)\tilde{c}_1(\tau) + \int_0^t d\tau\frac{\mathbf{d_0}\cdot\mathbf{E}(\tau)}{\hbar}\tilde{c}_2^\dagger(\tau)D_+(\tau)D_-(t)\\ &\times\int_0^t d\tau' e^{-i(\omega_A-\Delta)(t-\tau')}\frac{\mathbf{d_0}\cdot\mathbf{E}(\tau')}{\hbar}D_+(\tau')\tilde{c}_1(\tau'). \end{aligned}\qquad\text{(A1)}$$

On the other hand, since $\tilde{c}_1^\dagger(0) = \tilde{c}_1^\dagger(\tau) + i\int_0^\tau d\tau'\frac{\mathbf{d_0}\cdot\mathbf{E}(\tau')}{\hbar}\tilde{c}_2^\dagger(\tau')D_+(\tau')$ and $\tilde{c}_2(0) = \tilde{c}_2(\tau)e^{i(\omega_A-\Delta)\tau} - i\int_0^\tau d\tau' e^{i(\omega_A-\Delta)\tau'}\frac{\mathbf{d_0}\cdot\mathbf{E}(\tau')}{\hbar}D_+(\tau')\tilde{c}_1(\tau')$,

$$\begin{aligned}\tilde{c}_1^\dagger(t)D_-(t)\tilde{c}_2(t) = {}& \tilde{c}_1^\dagger(0)D_-(t)\tilde{c}_2(0)e^{-i(\omega_A-\Delta)(t-\tau)} - i\int_0^t d\tau e^{-i(\omega_A-\Delta)(t-\tau)}\frac{\mathbf{d_0}\cdot\mathbf{E}(\tau)}{\hbar}\tilde{c}_2^\dagger(\tau)D_+(\tau)D_-(t)\tilde{c}_2(\tau)\\ &-\int_0^t d\tau e^{-i(\omega_A-\Delta)t}\frac{\mathbf{d_0}\cdot\mathbf{E}(\tau)}{\hbar}\tilde{c}_2^\dagger(\tau)D_+(\tau)D_-(t)\left[\int_0^\tau d\tau' e^{i(\omega_A-\Delta)\tau'}\frac{\mathbf{d_0}\cdot\mathbf{E}(\tau')}{\hbar}D_+(\tau')\tilde{c}_1(\tau')\right]\\ &+i\int_0^t d\tau e^{-i(\omega_A-\Delta)(t-\tau)}\frac{\mathbf{d_0}\cdot\mathbf{E}(\tau)}{\hbar}\tilde{c}_1^\dagger(\tau)D_-(t)D_+(\tau)\tilde{c}_1(\tau) - \int_0^t d\tau e^{-i(\omega_A-\Delta)(t-\tau)}\frac{\mathbf{d_0}\cdot\mathbf{E}(\tau)}{\hbar}\end{aligned}$$

$$\begin{aligned}
&\times\left[\int_0^\tau d\tau' \frac{\mathbf{d_0}\cdot\mathbf{E}(\tau')}{\hbar}\tilde{c}_2^\dagger(\tau')D_+(\tau')\right]D_-(t)D_+(\tau)\tilde{c}_1(\tau)+\int_0^t d\tau\frac{\mathbf{d_0}\cdot\mathbf{E}(\tau)}{\hbar}\tilde{c}_2^\dagger(\tau)D_+(\tau)D_-(t)\\
&\times\int_0^t d\tau' e^{-i(\omega_A-\Delta)(t-\tau')}\frac{\mathbf{d_0}\cdot\mathbf{E}(\tau')}{\hbar}D_+(\tau')\,\tilde{c}_1(\tau')\\
={}&\tilde{c}_1^\dagger(0)D_-(t)\tilde{c}_2(0)e^{-i(\omega_A-\Delta)(t-\tau)}-i\int_0^t d\tau e^{-i(\omega_A-\Delta)(t-\tau)}\frac{\mathbf{d_0}\cdot\mathbf{E}(\tau)}{\hbar}\left[\tilde{c}_2^\dagger(\tau)D_+(\tau)D_-(t)\tilde{c}_2(\tau)\right.\\
&\left.-\tilde{c}_1^\dagger(\tau)D_-(t)D_+(\tau)\tilde{c}_1(\tau)\right]-\int_0^t d\tau\int_0^\tau d\tau' f(t,\tau,\tau')-\int_0^t d\tau'\int_0^{\tau'} d\tau f(t,\tau,\tau')\quad(\tau\leftrightarrow\tau')\\
&+\int_0^t d\tau\int_0^t d\tau' f(t,\tau,\tau'),
\end{aligned}\tag{A2}$$

where

$$f(t,\tau,\tau')=e^{-i(\omega_A-\Delta)(t-\tau')}\frac{\mathbf{d_0}\cdot\mathbf{E}(\tau)}{\hbar}\frac{\mathbf{d_0}\cdot\mathbf{E}(\tau')}{\hbar}\tilde{c}_2^\dagger(\tau)D_+(\tau)D_-(t)D_+(\tau')\tilde{c}_1(\tau').\tag{A3}$$

Using $\int_0^t d\tau\int_0^t d\tau' f(t,\tau,\tau')=\int_0^t d\tau\int_0^\tau d\tau' f(t,\tau,\tau')+\int_0^t d\tau'\int_0^{\tau'} d\tau f(t,\tau,\tau')$, we obtain

$$\begin{aligned}
\tilde{c}_1^\dagger(t)D_-(t)\tilde{c}_2(t)={}&\tilde{c}_1^\dagger(0)D_-(t)\tilde{c}_2(0)e^{-i(\omega_A-\Delta)(t-\tau)}\\
&-i\int_0^t d\tau e^{-i(\omega_A-\Delta)(t-\tau)}\frac{\mathbf{d_0}\cdot\mathbf{E}(\tau)}{\hbar}\\
&\times\left[\tilde{c}_2^\dagger(\tau)D_+(\tau)D_-(t)\tilde{c}_2(\tau)\right.\\
&\left.-\tilde{c}_1^\dagger(\tau)D_-(t)D_+(\tau)\tilde{c}_1(\tau)\right].
\end{aligned}\tag{A4}$$

The square integral region of $0\leqslant\tau\leqslant t$ and $0\leqslant\tau'\leqslant t$ can be separated into lower and upper triangular integral regions divided by $\tau=\tau'$. $\int_0^t d\tau\int_0^\tau d\tau'$ and $\int_0^t d\tau'\int_0^{\tau'} d\tau$ correspond to the integrals in the lower and upper triangular regions, respectively.

[1] S. John, Phys. Rev. Lett. **58**, 2486 (1987).
[2] E. Yablonovitch, Phys. Rev. Lett. **58**, 2059 (1987).
[3] S. John, Phys. Rev. Lett. **53**, 2169 (1984).
[4] A. Mekis, J. C. Chen, I. Kurland, S. Fan, P. R. Villeneuve, and J. D. Joannopoulos, Phys. Rev. Lett. **77**, 3787 (1996).
[5] P. R. Villeneuve, S. Fan, and J. D. Joannopoulos, Phys. Rev. B **54**, 7837 (1996).
[6] S. Fan, P. R. Villeneuve, J. D. Joannopoulos, and H. A. Haus, Phys. Rev. Lett. **80**, 960 (1998).
[7] A. Mekis, S. Fan, and J. D. Joannopoulos, Phys. Rev. B **58**, 4809 (1998).
[8] A. Chutinan and S. Noda, Appl. Phys. Lett. **75**, 3739 (1999).
[9] A. Chutinan, S. John, and O. Toader, Phys. Rev. Lett. **90**, 123901 (2003).
[10] A. Chutinan and S. John, Phys. Rev. E **71**, 026605 (2005).
[11] E. M. Purcell, Phys. Rev. **69**, 681 (1946).
[12] M. Florescu and S. John, Phys. Rev. A **64**, 033801 (2001).
[13] S. John and M. Florescu, J. Opt. A Pure Appl. Opt. **3**, S103 (2001).
[14] M. Florescu and S. John, Phys. Rev. A **69**, 053810 (2004).
[15] X. Ma and S. John, Phys. Rev. Lett. **103**, 233601 (2009).
[16] X. Ma and S. John, Phys. Rev. A **80**, 063810 (2009).
[17] B. R. Mollow, Phys. Rev. **188**, 1969 (1969).
[18] S. John and T. Quang, Phys. Rev. Lett. **78**, 1888 (1997).
[19] D. Vujic and S. John, Phys. Rev. A **76**, 063814 (2007).
[20] R. Z. Wang and S. John, Phys. Rev. A **70**, 043805 (2004).
[21] K. Busch and S. John, Phys. Rev. E **58**, 3896 (1998).
[22] A. Taflove and S. C. Hagness, *Computational Electrodynamics: The Finite-Difference Time-Domain Method* 3rd ed., (Artech House, Boston, 2005).
[23] L. Allen and J. H. Eberly, *Optical Resonance and Two-Level Atoms* (Dover, New York, 1987).
[24] G. Slavcheva, J. M. Arnold, I. Wallace, and R. W. Ziolkowski, Phys. Rev. A **66**, 063418 (2002).
[25] H. Oka, S. Takeuchi, and K. Sasaki, Phys. Rev. A **72**, 013816 (2005).
[26] A. Fratalocchi, C. Conti, and G. Ruocco, Phys. Rev. A **78**, 013806 (2008).
[27] Y. Niu, K. Xia, N. Cui, S. Gong, and R. Li, Phys. Rev. A **78**, 063835 (2008).
[28] B. Krummheuer, V. M. Axt, and T. Kuhn, Phys. Rev. B **65**, 195313 (2002).
[29] G. D. Mahan, *Many Particle Physics* (Plenum, New York, 1990).
[30] C. Roy and S. John, Phys. Rev. A **81**, 023817 (2010).
[31] N. Vats and S. John, Phys. Rev. A **58**, 4168 (1998).
[32] L. K. Yu, B. Xu, Z. G. Wang, P. Jin, C. Zhao, W. Lei, J. Sun, K. Li, L. J. Hu, and L. Y. Liang, J. Cryst. Growth **282**, 173 (2005).
[33] K. Akahane, N. Yamamoto, and M. Tsuchiya, Appl. Phys. Lett. **93**, 041121 (2008).
[34] G. Khitrova, H. M. Gibbs, M. Kira, S. W. Koch, and A. Scherer, Nat. Phys. **2**, 81 (2006).
[35] B. K. Ridley, *Quantum Processes in Semiconductors* (Clarendon, Oxford, 1999).

[36] S. Rudin, T. L. Reinecke, and M. Bayer, Phys. Rev. B **74**, 161305(R) (2006).

[37] P. Borri, W. Langbein, S. Schneider, U. Woggon, R. L. Sellin, D. Ouyang, and D. Bimberg, Phys. Rev. Lett. **87**, 157401 (2001).

[38] S. G. Johnson, P. Bienstman, M. A. Skorobogatiy, M. Ibanescu, E. Lidorikis, and J. D. Joannopoulos, Phys. Rev. E **66**, 066608 (2002).

[39] E. H. Khoo, A. Q. Liu, and J. H. Wu, Opt. Express **13**, 7742 (2005).